Supplementary Information for:

Rattle Drum Inspired Triboelectric Nanogenerator Achieving a Record Triboelectric Surface Density of 2.76 cm^{-1}

Wei Tang,[ab] Hongfang Li,[ab] Jiawei Li,[ab] Weiyu Zhou,[ab] Jiaqi Duan,[ab] Yongsheng Wen,[ab] Lingyu Wan,*[ab] and Guanlin Liu*[ab]

[a]Center on Nanoenergy Research, Institute of Science and Technology for Carbon Peak & Neutrality, School of Physical Science & Technology, Guangxi University, Nanning 530004, China. Email address: lyw2017@gxu.edu.cn (Lingyu Wan), guanlinliu@gxu.edu.cn (Guanlin Liu)

[b]State Key Laboratory of Featured Metal Materials and Life-cycle Safety for Composite Structures, Guangxi University, Nanning 530004, China

Keywords: High-Density Triboelectric Layer, Charge Dispatch Strategy, Three-Electrode, Triboelectric Nanogenerator, Frequency-Reducing and Amplitude-Amplifying Magnetic Repulsion Pendulum, Wave Energy.

Content

Supplementary Table

Table S1. Comparison of the RD-TENG with other works in terms of unit volume output charge density, specific surface area density, friction layer area-to-mass ratio, and peak power density.

Table S2. Comparison of RD-TENG output with traditional FCS structures.

Supplementary Note

Note S1. The difficulties arise after the densification of friction layers in traditional FCS-TENG.

Note S2. The three-electrode configuration of the RD-TENG.

Note S3. Orthogonal experimental design.

Supplementary Figures

Figure S1. (a) Photograph of the rattle-drum. (b) rattle-drum-type TENG

Figure S2. Charge dispatch and transfer schematic diagram for each electrode pair of RD-TENG. (a) 1-3 electrode pair. (b) 1-2 electrode pair. (c) 2-3 electrode pair. (d) rectified electrode pair.

Figure S3. (a) Simulation of the electric potential of the vibrating sheet moving from one end to the other in the RD-TENG. (b) Positions of each electrode and their electric potential variation curves as the vibrating sheet oscillates from one end to the other.

Figure S4. Three-electrode rectifier circuit diagram and its physical circuit image.

Figure S5. Vibration sheet style, parameters, model, and physical image.

Figure S6. Vibration simulation of the vibrating steel sheet.

Figure S7. Packaged device model parameters and physical image.

Figure S8. Packaged device model parameters and physical image.

Figure S9. Acrylic ring gasket parameters, model, and physical image.

Figure S10. Push pin and latch parameters.

Figure S11. Bottom sealing plate and its parameters.

Figure S12. The protruding end of the push pin serves as the electrode lead-out terminal.

Figure S13. Electrode conductive sheet parameters, position, model, and physical image.

Figure S14. Packaging barrel parameters and its physical image.

Figure S15. Top sealing plate and its parameters.

Figure S16. Conductive sponge and its installation location.

Figure S17. Assembly steps of RD-TENG device.

Figure S18. Parameters and physical image of the rotating-clasp-device.

Figure S19. (a) Details and physical image of the RD-TENG device array. (b) Connection method of push-pin electrodes in the device array.

Figure S20. Vibrational energy simulation testing platform.

Figure S21. Comparison of the output of RD-TENG (Structure 4) with traditional structures. (a-c) Comparison of output charge, current, and voltage for the 1-2 electrode pair across different structures. (d-f) Comparison of output charge, current, and voltage for the 2-3 electrode pair across different structures. (g-h) Comparison of output charge, current, and voltage for the rectified electrode pair across different structures.

Figure S22. Output characteristics of RD-TENG. (a) Cumulative charge of the rectified electrode pair of RD-TENG under optimal excitation conditions. (b-c) Short-circuit current and open-circuit voltage of each electrode pair. (d) The relationship between charge output of each electrode pair and amplitude under a frequency of 2.4 Hz. (e) The output relationship between the output quantities of the 2-3 electrode pair and the amplitude under a frequency of 2.4 Hz.

Figure S23. Output characteristics of RD-TENG for harvesting vibrational energy. (a) Array device vibration energy simulation testing platform (b-c) Under the optimal excitation conditions of frequency 2.4 Hz and amplitude 70 mm, the output relationship of short-circuit current and open-circuit voltage with the increase in the number of device arrays. (d) The output relationship of the 1-2 electrode pair for three devices within the array under optimal excitation conditions concerning the variation of azimuth angle. (e-i) Vertical test platform and short-circuit transfer charge, open-circuit voltage, short-circuit current of each electrode pair in vertical testing. (j-l) Output voltage, current, and peak power density of RD-TENG with different load resistances for the 1-2, 2-3, and rectified electrode pairs.

Figure S24. Application of RD-TENG for vibration energy harvesting. (a) One RD-TENG device charges a 100 μF capacitor for 100 seconds, drives two parallel calculators with continuous power supply for 15 seconds. (b) Schematic diagram showing the lighting of 32 2 W LED bulbs from dim to bright by adding 1 to 4 devices in sequence in the array under the optimal combination of 2.4 Hz frequency and 70 mm amplitude. (c) RD-TENG illuminates 32 2W LED bulbs under vertical drive. (d) The rectifier electrode pair of a single RD-TENG device is placed in the bicycle front basket, driving five 2W commercial LED bulbs as a front light or warning light for the bicycle, providing safety warnings for night rides.

Figure S25. Dimensional parameters and schematic diagram of the components of frequency-reducing and amplitude-amplifying magnetic repulsion pendulum.

Figure S26. RD-TENG based on frequency-reducing and amplitude-amplifying magnetic repulsion pendulum driven by a six-degree-of-freedom platform. (a) linear drive. (b) swinging drive.

Figure S27. Amplitude amplification calculation diagram of frequency-reducing and amplitude-amplifying magnetic repulsion pendulum under linear and swinging drive. (a) linear drive. (b) swinging drive.

Figure S28. Output characteristics of RD-TENG based on frequency-reducing and amplitude-amplifying magnetic repulsion pendulum under linear drive and swing drive on a six-degree-of-freedom platform. (a-c) Short-circuit transferred charge, open-circuit voltage, and short-circuit current of each electrode pair under linear drive. (d-f) Short-circuit transferred charge, open-circuit voltage, and short-circuit current of each electrode pair under swinging drive. (g-h) Relationship between output quantities and frequency (Fixed at an amplitude of 70 mm), amplitude (Fixed at a frequency of 2.4 Hz) under linear drive. (i) Frequency reduction and amplitude amplification characteristics under linear drive. (j-k) Relationship between output quantities and frequency (Fixed at an amplitude 70 mm), amplitude (Fixed at a frequency of 2.4 Hz) under swinging drive. (l) Frequency reduction and amplitude amplification characteristics under swinging drive.

Figure S29. Force analysis diagram of the vibrating sheet under swinging drive, where a larger swing angle allows the rotor to open more effectively.

Figure S30. Comparison of 1-3 and rectified electrode pair lighting up 64 2 W LED bulbs in linear drive and swinging drive mode of RD-TENG based on the frequency-reducing and amplitude-amplifying magnetic repulsion pendulum.

Figure S31. Durability test of the 1-3 electrode pair of RD-TENG based on low-frequency and amplitude-amplifier of magnetic repulsive pendulum under linear excitation.

Figure S32. Diagram of the unbalanced gravity pendulum set on the edge of a buoyant base.

Figure S33. Wave amplitudes and frequencies generated by different modes in a wave pool.

Figure S34. Satellite location map of the Beibu Gulf test base.

Supplementary Movies

Movie S1. Assembly of the RD-TENG device array connection.

Movie S2. The RD-TENG powers two parallel calculators.

Movie S3. An array of four-RD-TENG powers two multimeters, one of which measures the voltage of a 1.5 V battery.

Movie S4. Comparison of rectified electrode pairs lighting 32 × 2 W LED bulbs after sequentially adding 1 to 4 RD-TENGs in the array.

Movie S5. The RD-TENG powers 5 × 2 W LED bulbs as a bicycle night-riding warning light.

Movie S6. The RD-TENG system lights up a "GXU" sign composed of 284 LED lights connected in series in a wave tank.

Movie S7. The RD-TENG system powers a temperature and humidity sensor in a wave tank.

Movie S8. The RD-TENG system operates under real ocean conditions.

Movie S9. The RD-TENG system powers two calculators on the sea surface after the ebb tide.

Table S1. Comparison of the RD-TENG with other works in terms of unit volume output charge density, specific surface area density, friction layer area-to-mass ratio, and peak power density.

Type	Reference	Charge (μC)	Friction area (cm^2)	Volume bulk (cm^3)	Weight (g)	Charge density ($mC\ m^{-3}$)	Specific Surface Area (cm^{-1})	Mass Surface Area ($cm^2\ g^{-1}$)	Peak power density ($W\ m^{-3}$)
RD-TENG	This work	6.33	999.35	361.73	345	11.69	2.76	2.9	1-3 electrode pair 136.74 1-2 electrode pair 102.51 2-3 electrode pair 84.97 Rectified electrode pair 114
FH-TENG	Ref. [26] 2025	7.9	2052.75	769.69	621.2	10.26	2.67	3.3	14.94
OM-TENG	Ref. [27] 2024	60.82	15226.63	8651.49	7110	7.03	1.76	2.14	28.9
SO-TENG	Ref. [28] 2024	1.5	900	1359.78	800	1.1	0.66	1.13	4.44
D-Z-TENG	Ref. [29] 2024	1.2	360	267	500	4.49	1.35	0.72	55.4
DA-TENG	Ref. [30 2024	1.8	343	/	/	0.19	0.8	/	7.51
GA-TENG	Ref. [31] 2024	/	/	/	/	/	/	/	20.4
LI-TENGs	Ref. [32] 2023	0.76	216	108	115.6	7	2	1.87	48.47
T-TENG	Ref. [33] 2023	1.15	460.86	430.71	358	2.67	1.07	1.29	18.9
HM-TENG	Ref. [34] 2022	67.2	951.72	924	742.6	2	1.03	1.28	2.44
O-TENG	Ref. [35] 2022	29.93	12160	6170.73	7300	4.85	1.97	1.67	1.62
MH-TENG	Ref. [36] 2023	2.9	783.78	698.28	353.25	4.15	1.12	2.2	23.2
D-TENG	Ref. [37] 2022	0.87	480	5400	280.8	0.16	0.09	1.71	6.35
S-TENG	Ref. [38] 2022	0.16	62.8	448	121.1	0.36	0.14	0.52	7.39
F-TENG	Ref. [39] 2022	0.18	65	2574.26	80.96	0.07	0.03	0.8	16.96
SR-TENG	Ref. [40] 2022	0.15	202.3	736.63	281	0.2	0.27	0.72	15.4

Table S2. Comparison of RD-TENG output with traditional FCS structures.

Comparison	Frequency (Hz)	1-3 electrode pair			1-2 electrode pair			2-3 electrode pair			rectified electrode pair.		
		Voltage (V)	Current (μA)	Charge (nC)	Voltage (V)	Current (μA)	Charge (nC)	Voltage (V)	Current (μA)	Charge (nC)	Voltage (V)	Current (μA)	Charge (nC)
Structure 1	0.8	27	0.51	10	39	0.72	10	41	0.58	9	22	1.18	167
	1.2	84	4.46	73	236	13.44	117	196	8.12	88	146	20.14	668
	1.6	272	22.13	137	492	60.65	325	364	34.68	315	256	66.04	1820
	2	440	26.58	150	592	78.63	402	424	76.41	396	328	77.86	2388
	2.4	480	31.92	164	760	83.23	488	792	71.64	378	648	81.75	3058
Structure 2	0.8	63	0.35	10	84	1.34	15	56	1.24	11	44	1.63	271
	1.2	204	3.27	46	96	2.46	30	292	7.74	85	304	22.2	1357
	1.6	416	16.92	168	584	36.14	285	460	63.4	424	448	34	1645
	2	900	22.62	179	640	54.1	316	700	100.46	597	576	71.06	2285
	2.4	1240	30.76	191	720	93.09	523	860	104.93	570	780	107.6	3254
Structure 3	0.8	272	2.75	71	/	/	/	/	/	/	/	/	/
	1.2	544	5.91	144	/	/	/	/	/	/	/	/	/
	1.6	1100	14.43	271	/	/	/	/	/	/	/	/	/
	2	1400	20	284	/	/	/	/	/	/	/	/	/
	2.4	1640	29.79	303	/	/	/	/	/	/	/	/	/
RD-TENG	0.8	264	2.91	77	180	3.14	78	116	2.75	73	124	2.37	433
	1.2	920	32.92	262	560	40.26	227	496	41.37	576.89	660	32.11	1458.4
	1.6	1420	70.22	951	740	96.43	1080	576	115.41	1215.24	840	77.41	2433.8
	2	1700	80.14	1326	940	144.92	1552	960	254.48	2643.62	960	118.2	3226
	2.4	2200	94	1903	1360	182	2595	1220	314.69	3275.2	1080	272	5480

Note S1. The difficulties arise after the densification of friction layers in traditional FCS-TENG.

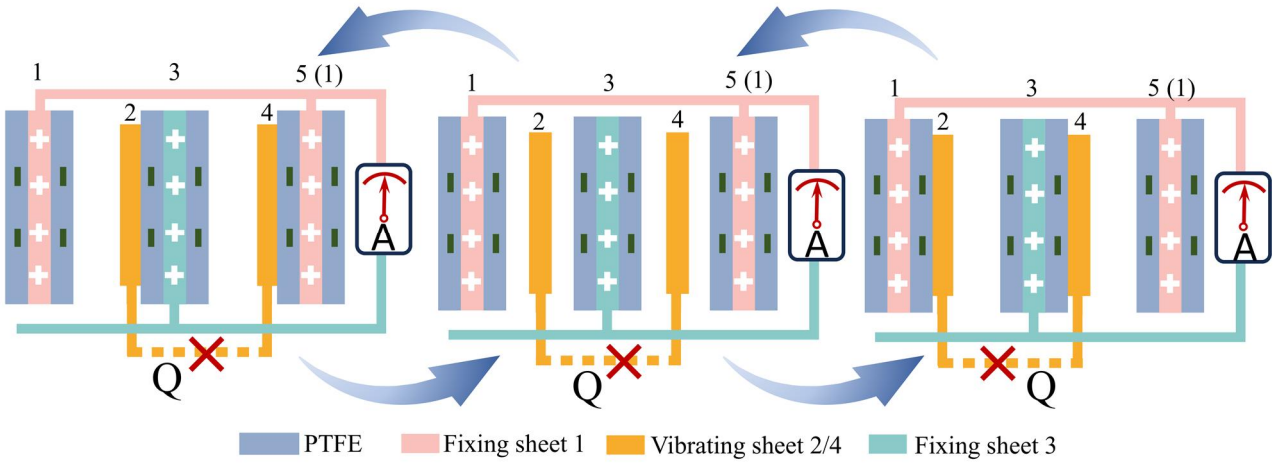

In the traditional free-standing layer vertical contact-separation mode TENG (FCS-TENG), when the array is stacked beyond two structural cycles, issues such as electrostatic shielding and low potential difference arise. For the fixing sheet 3, when the mover on the vibrating sheet 2 approaches it, the mover on the vibrating sheet 4 moves away, and vice versa. This means that at any given moment, the fixing sheet 3 always has one mover approaching and one mover moving away. However, because there is no mechanism for charge compensation and migration between the movers on vibrating sheets 2 and 4, and due to the electrostatic shielding effect within the gap, caused by the completely symmetric film coating and arrangement in the dense stacking of fixing sheets 1 and 3, the electric potential between movers 2 and 4 remains unchanged. As a result, the electric potential on fixing sheet 3 also remains almost constant, and the same applies to other fixing sheets. In summary, the lack of a charge migration pathway between movers 2 and 4, combined with the electrostatic shielding from dense stacking and the small contact-separation distance within the dense layers, prevents the generation of a varying potential field. This leads to an inability to create a high potential difference between the output channels of layers 1 and 3, resulting in minimal charge transfer between electrodes 1 and 3 and almost no current flow in the circuit.

Note S2. The three-electrode configuration of the RD-TENG.

Based on the principle of the rattle-drum-type charge dispatch strategy, we optimized the film-coating method for the spring steel sheets: single-sided film coating on the fixed sheets, non-coated vibrating sheets, and full-coated vibrating sheets. These are arranged in the following order (from left to right): right-coated fixed sheet, non-coated vibrating sheet, left-coated fixed sheet, full-coated vibrating sheet, and right-coated fixed sheet (with another structure cycle starting), and sequence forms three electrodes with alternating coatings. The three-electrode configuration of the RD-TENG is designed to enhance charge dispatch efficiency by mimicking the structure and function of a rattle drum. Electrode 1 consists entirely of fixed sheets with right-side coatings, serving as a primary charge collection component. Electrode 2 is composed of two types of vibrating sheets—non-coated and fully coated—which are electrically short-circuited together. These vibrating sheets function similarly to the two pendulums in a rattle drum, facilitating charge redistribution during operation. Electrode 3 is made up of fixed sheets with left-side coatings, acting as another key charge collection component. Notably, the fixed sheets in electrodes 1 and 3 correspond to the two opposite sides of a rattle drum, further reinforcing the mechanical-electrical analogy embedded in the RD-TENG design.

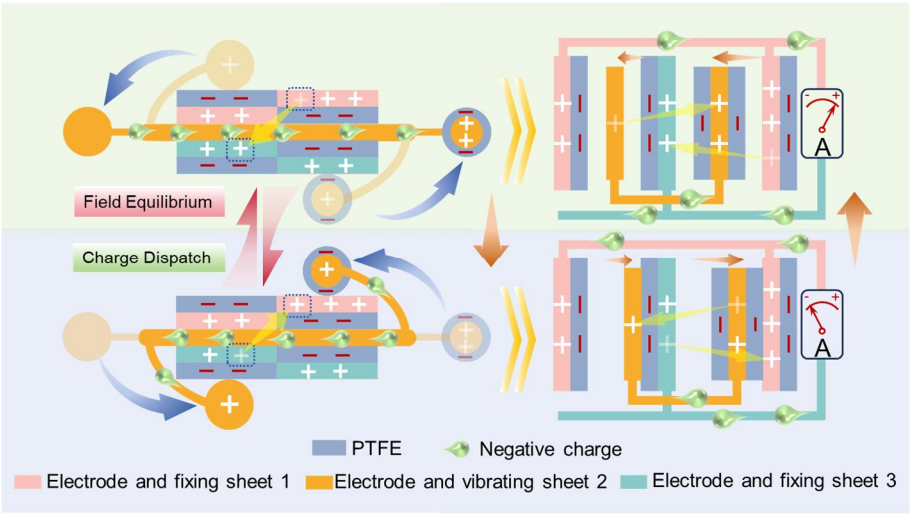

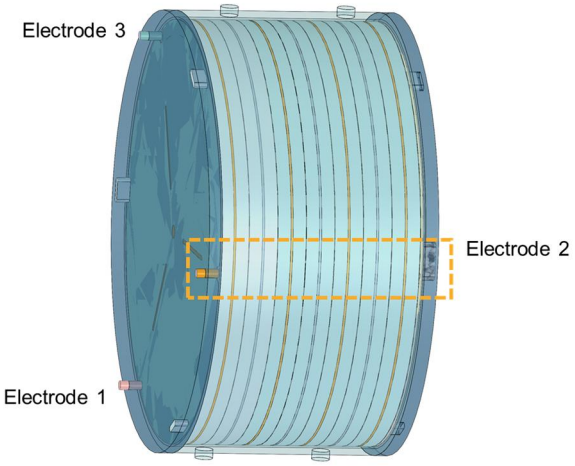

Note S3. Orthogonal experimental design.

Introduction

The output of RD-TENG is not only influenced by amplitude and acceleration individually but may also be affected by the interaction between amplitude and acceleration. To scientifically determine the optimal output frequency combination, the best output, and the hierarchical relationships between parameters, we introduced the orthogonal experimental method to systematically explore the optimal combinations of amplitude, acceleration, and terminal velocity. This approach allows us to derive the optimal frequency-to-amplitude ratio. To systematically investigate the response patterns of the device to various input excitation parameters, and to better understand the mechanical-to-electrical energy conversion capability of the RD-TENG, as well as the influencing factors and their hierarchical relationships, we applied the orthogonal experimental method commonly used in engineering applications to study linear and oscillatory excitation input parameters. [43, 44]

The orthogonal experimental method is a widely used experimental design approach in engineering applications. Systematically arranging and analyzing multi-factor and multi-level experiments it helps optimize and improve products or processes. The basic principle is to use orthogonal tables to reasonably combine experimental factors and levels, ensuring that both the main effects and interaction effects of each factor are effectively evaluated. The core idea is to leverage the orthogonality of the orthogonal table to balance the factor combinations, thereby reducing the number of experiments while ensuring the representativeness and reliability of the results. Orthogonal tables are characterized by "uniform distribution and neat comparability," which allows for effective separation of factor effects and their interactions, making them suitable for optimizing process parameters, product design, and other fields.

With the assistance of the orthogonal experimental method, the external excitation input parameters that influence the output of the RD-TENG were systematically explored and optimized. This method has significantly advanced subsequent tests and research. Furthermore, the orthogonal experimental method introduced in this study can inspire researchers in the industry by providing methodologies and approaches for finding the optimal combinations in TENG device structure design, energy harvesting system optimization, and power management with multi-component coupling, particularly in research involving multiple variables and parameters.

Experiment 1: Orthogonal experimental design of RD-TENG under direct linear drive.

1. **Clarify the purpose of the experiment.**

Select the optimal combination from the input parameters of the linear motor, including wave frequency, wave amplitude, acceleration, and terminal velocity. Ultimately, determine the best input and output for the device, as well as the primary and secondary relationships among the input parameters.

Table N1. Factor-level table.

Num.	Factors	Levels		Index	Orthogonal table
		Range	Acquisition quantity	2-3 electrode pair	
1	Frequency (Hz)	Obtain the optimal quantity	1	Short-circuit transfer charge: Q	$L_{49}(7^8)$
2	Amplitude (mm)	10-70	7		
3	Acceleration (m s^{-2})	1-13	7		
4	Terminal velocity (m s^{-1})	2-8	7		

2. Determine the factors, levels, and indices, and select the orthogonal table.

Table N2. Orthogonal table.

Experiment Num. \ Row Num.	1	2	3	4	5	6	7	8
1	1	1	1	1	1	1	1	1
2	1	2	2	2	2	2	2	2
3	1	3	3	3	3	3	3	3
4	1	4	4	4	4	4	4	4
5	1	5	5	5	5	5	5	5
6	1	6	6	6	6	6	6	6
7	1	7	7	7	7	7	7	7
8	2	1	2	3	4	5	6	7
9	2	2	3	4	5	6	7	1
10	2	3	4	5	6	7	1	2
11	2	4	5	6	7	1	2	3
12	2	5	6	7	1	2	3	4
13	2	6	7	1	2	3	4	5
14	2	7	1	2	3	4	5	6
15	3	1	3	5	7	2	4	6
16	3	2	4	6	1	3	5	7
17	3	3	5	7	2	4	6	1
18	3	4	6	1	3	5	7	2
19	3	5	7	2	4	6	1	3
20	3	6	1	3	5	7	2	4
21	3	7	2	4	6	1	3	5
22	4	1	4	7	3	6	2	5
23	4	2	5	1	4	7	3	6
24	4	3	6	2	5	1	4	7
25	4	4	7	3	6	2	5	1
26	4	5	1	4	7	3	6	2
27	4	6	2	5	1	4	7	3
28	4	7	3	6	2	5	1	4
29	5	1	5	2	6	3	7	4
30	5	2	6	3	7	4	1	5
31	5	3	7	4	1	5	2	6
32	5	4	1	5	2	6	3	7

Table Continued.

Experiment Num. \ Row Num.	1	2	3	4	5	6	7	8
33	5	5	2	6	3	7	4	1
34	5	6	3	7	4	1	5	2
35	5	7	4	1	5	2	6	3
36	6	1	6	4	2	7	5	3
37	6	2	7	5	3	1	6	4
38	6	3	1	6	4	2	7	5
39	6	4	2	7	5	3	1	6
40	6	5	3	1	6	4	2	7
41	6	6	4	2	7	5	3	1
42	6	7	5	3	1	6	4	2
43	7	1	7	6	5	4	3	2
44	7	2	1	7	6	5	4	3
45	7	3	2	1	7	6	5	4
46	7	4	3	2	1	7	6	5
47	7	5	4	3	2	1	7	6
48	7	6	5	4	3	2	1	7
49	7	7	6	5	4	3	2	1

3. **Header design.**

Table N3. Table header design of experiment 1.

Factors	Acceleration (m s^{-2})	Amplitude (mm)	Terminal velocity (m s^{-1})	/	/	/	/	/	Results
	A	B	C	/	/	/	/	/	2-3: Q (nC)
Num.	1	2	3	4	5	6	7	8	/

4. **Design experimental scheme.**

Table N4. Experimental setup and data acquisition.

Experiment Num. \ Row Num.	1	2	3	4	5	6	7	8	Results
	Acceleration: a (m s^{-2})	Amplitude: A (mm)	Terminal velocity: v (m s^{-1})	/	/	/	/	/	1-2: Q (nC)
1	3	10	2	/	/	/	/	/	74
2	3	20	3	/	/	/	/	/	193
3	3	30	4	/	/	/	/	/	125
4	3	40	5	/	/	/	/	/	103
5	3	50	6	/	/	/	/	/	131
6	3	60	7	/	/	/	/	/	246
7	3	70	8	/	/	/	/	/	114
8	5	10	3	/	/	/	/	/	686
9	5	20	4	/	/	/	/	/	743
10	5	30	5	/	/	/	/	/	456
11	5	40	6	/	/	/	/	/	500
12	5	50	7	/	/	/	/	/	736
13	5	60	8	/	/	/	/	/	738
14	5	70	2	/	/	/	/	/	469
15	7	10	4	/	/	/	/	/	1,290
16	7	20	5	/	/	/	/	/	1,261
17	7	30	6	/	/	/	/	/	1,074
18	7	40	7	/	/	/	/	/	1,084
19	7	50	8	/	/	/	/	/	1,212

Table Continued.

Row Num. / Experiment Num.	1	2	3	4	5	6	7	8	Results
	Acceleration: a (m s^{-2})	Amplitude: A (mm)	Terminal velocity: v (m s^{-1})	/	/	/	/	/	1-2: Q (nC)
20	7	60	2	/	/	/	/	/	1,233
21	7	70	3	/	/	/	/	/	1,122
22	9	10	5	/	/	/	/	/	903
23	9	20	6	/	/	/	/	/	1,137
24	9	30	7	/	/	/	/	/	1,487
25	9	40	8	/	/	/	/	/	1,285
26	9	50	2	/	/	/	/	/	1,558
27	9	60	3	/	/	/	/	/	1,354
28	9	70	4	/	/	/	/	/	1,558
29	11	10	6	/	/	/	/	/	933
30	11	20	7	/	/	/	/	/	1,573
31	11	30	8	/	/	/	/	/	1,637
32	11	40	2	/	/	/	/	/	1,716
33	11	50	3	/	/	/	/	/	1,451
34	11	60	4	/	/	/	/	/	1,790
35	11	70	5	/	/	/	/	/	1,845
36	13	10	7	/	/	/	/	/	1,286
37	13	20	8	/	/	/	/	/	1,721
38	13	30	2	/	/	/	/	/	1,953
39	13	40	3	/	/	/	/	/	1,970
40	13	50	4	/	/	/	/	/	1,628
41	13	60	5	/	/	/	/	/	1,802
42	13	70	6	/	/	/	/	/	2,089
43	15	10	8	/	/	/	/	/	1,105
44	15	20	2	/	/	/	/	/	1,664
45	15	30	3	/	/	/	/	/	1,854
46	15	40	4	/	/	/	/	/	1,787
47	15	50	5	/	/	/	/	/	1,907
48	15	60	6	/	/	/	/	/	2,004
49	15	70	7	/	/	/	/	/	2,141

5. The calculation method of the mean analysis in orthogonal experimental design.

In orthogonal experimental design, the range analysis method is mainly used to assess the influence of factors on experimental results by comparing the ranges (the difference between the maximum and minimum values) of the data. The calculation method involves the following steps:

1) Organize experimental data.

Before performing range analysis, the orthogonal experiment should be completed, and the results should be recorded. The original data acquisition is shown in the figure below.

2) Calculate the average evalue for each factor level.

For each factor at different levels, calculate the average value of all experimental results. Suppose a factor has k levels, and the experimental results at each level are y_{ji} (where j=1, 2, …, k. i = 1, 2, …, m., and m is the number of experiments at each level).

Calculate the average value at each level as follows:

$$\bar{y}_j = \frac{1}{m}\sum_{i=1}^{m} y_{ji}$$

where $\bar{y}_j$ is the average value at the *j-th* level of the factor.

3) Calculate the range for each factor.

For each factor, find the maximum and minimum values at each level and compute the range:

$$R_j = \max(\bar{y}_j) - \min(\bar{y}_j)$$

Where R_j is the range of factor *j,* representing the fluctuation range of the experimental results for that factor.

4) Compare the ranges of different factors.

Compare the ranges of all factors. A larger range indicates a greater influence on the experimental results, helping to identify significant factors.

5) Determine the optimal factor level combination.

Based on the comparison of ranges, identify the most influential factors and their optimal levels.

6) Summary.

Through the range analysis method in orthogonal experimental design, the influence of multiple factors on experimental results can be quickly evaluated, and the optimal factor-level combination can be selected to optimize the experiment. This method is simple and efficient, and it is suitable for the preliminary screening and optimization of experiments with multiple factors.

Table N5. Data analysis.

Row Num. / Experiment Num.	1	2	3	4	5	6	7	8	Results
	Acceleration: a (m s^{-2})	Amplitude: A (mm)	Terminal velocity: v (m s^{-1})	/	/	/	/	/	1-3: Q (nC)
y_{j1}	985	6,277	8,667	/	/	/	/	/	/
y_{j2}	4,328	8,292	8,630	/	/	/	/	/	/
y_{j3}	8,276	8,586	8,921	/	/	/	/	/	/
y_{j4}	9,282	8,445	8,277	/	/	/	/	/	/
y_{j5}	10,945	8,623	7,868	/	/	/	/	/	/
y_{j6}	12,449	9,167	8,553	/	/	/	/	/	/
y_{j7}	12,462	9,338	7,812	/	/	/	/	/	/
$\bar{y}_{j1}$	141	897	1,238	/	/	/	/	/	/
$\bar{y}_{j2}$	618	1,185	1,233	/	/	/	/	/	/
$\bar{y}_{j3}$	1,182	1,227	1,274	/	/	/	/	/	/
$\bar{y}_{j4}$	1,326	1,206	1,182	/	/	/	/	/	/
$\bar{y}_{j5}$	1,564	1,232	1,124	/	/	/	/	/	/

Table Continued.

Row Num. / Experiment Num.	1 Acceleration: a (m s^{-2})	2 Amplitude: A (mm)	3 Terminal velocity: v (m s^{-1})	4 /	5 /	6 /	7 /	8 /	Results 1-3: Q (nC)
$\overline{y}_{j6}$	1,778	1,310	1,222	/	/	/	/	/	/
$\overline{y}_{j7}$	1,780	1,334	1,116	/	/	/	/	/	/
R_j	1,639	437	150	/	/	/	/	/	/
Trend analysis chart	Figure N1a.	Figure N1b.	Figure N1c.	/	/	/	/	/	/
Optimal combination	13	70	4	/	/	/	/	/	/
Primary and secondary factors	Acceleration ＞ Amplitude ＞ Terminal velocity								
Frequency conversion: f	f=2.4, $a = f^2 * 0.001 * 32 * A$								

Figure N1. The original data acquisition diagram of the orthogonal experimental design of RD-TENG under direct linear drive.

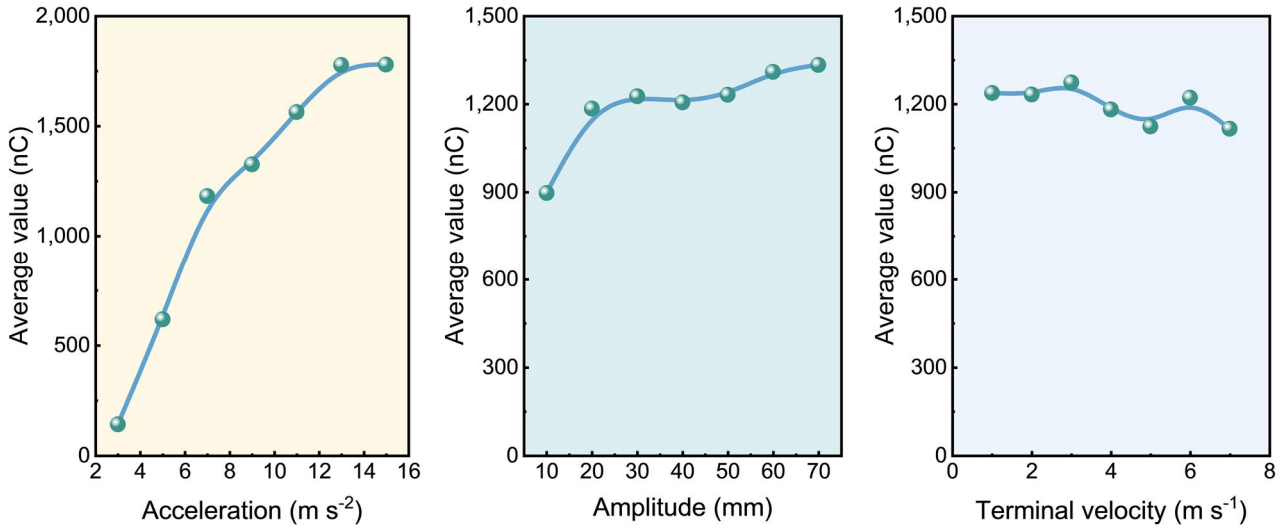

Figure N2. The output variation trend of RD-TENG under direct linear drive concerning each input parameter.

6. Conclusion.

The following conclusions were drawn based on range analysis: As the amplitude increases, the output initially increases rapidly, then slows down and tends to saturate. An increase in amplitude means that the vibrating sheet's movement distance becomes greater, allowing more time for the vibrating sheet to complete the contact-separation process with the fixing sheet and efficiently generate electricity. However, as the amplitude continues to increase, the contact-separation efficiency between the vibrating sheet and the fixing sheet gradually reaches an optimal state. When the amplitude reaches approximately 70 mm, the output stabilizes and no longer increases. The relationship between acceleration and output shows a peak: when the acceleration is 13 m s^{-2}, the output reaches its maximum value, after which the output slightly decreases as acceleration further increases. This is because, with constant amplitude, an increase in acceleration results in a rise in frequency. As the frequency increases, the contact-separation speed between the vibrating sheet and the fixing sheet accelerates. The moving part gains higher velocity, thus higher momentum, which leads to more thorough contact with the fixing sheet and an increased output. However, as the frequency continues to increase, the moving part cannot separate and return in time during the short duration, resulting in a decrease in output. The terminal velocity, as the frequency adjustment variable of the linear motor, has little effect on the output of the device. Ultimately, through comprehensive analysis, the optimal operating conditions of the RD-TENG are found to be at an amplitude of 70 mm, acceleration of 13 m s^{-2}, and terminal velocity of 4 m s^{-1}. The best output frequency, as calculated, is 2.4 Hz.

Experiment 2: Orthogonal experimental design of RD-TENG under linear drive and swinging drive based on frequency-reducing and amplitude-amplifying magnetic repulsion pendulum.

1. **Define the Experimental Objective:** The goal of the experiment is to select two optimal combinations from the six degrees of freedom input parameters: wave frequency, wave amplitude, amplitude coefficient, and swing angle. The first optimal combination is derived for the linear drive, including wave frequency, wave amplitude, and amplitude coefficient, while the second optimal combination corresponds to the swinging drive, which includes wave frequency, swing angle, and amplitude coefficient. Ultimately, the best inputs and outputs for the device in both linear drive and swinging drive states across the six degrees of freedom will be determined, along with the hierarchical relationships between the influence of each input parameter.

Table N6. Factor-level table.

Num.	Factors	Levels		Index	Experiment		
		Range	Acquisition quantity	1-3 electrode pair	Num.	Combination	Orthogonal table
1	Frequency (Hz)	0.6-1.8	7	Short-circuit transfer charge: Q	A	1,2,3	$L_{49}(7^8)$
2	Amplitude (mm)	8-20	7				
3	amplitude coefficient	1-7	7		B	1,4,3	$L_{49}(7^8)$
4	Pendulum angle (°)	0-30	7				

2. Determine the factors, levels, and indices, and select the orthogonal table.

The orthogonal table is the same as in Experiment 1.

3. **Header design.**

Table N7. Table header design of combination A for the linear drive of experiment 2.

Factors	Frequency (Hz)	Amplitude (mm)	Amplitude coefficient	/	/	/	/	/	Results
	A	B	C	/	/	/	/	/	1-3: Q (nC)
Num.	1	2	3	4	5	6	7	8	/

Table N8. Table header design of combination B for swinging drive of experiment 2.

Factors	Frequency (Hz)	Pendulum angle (°)	Amplitude coefficient	/	/	/	/	/	Results
	A	B	C	/	/	/	/	/	1-3: Q (nC)
Num.	1	2	3	4	5	6	7	8	/

4. Design an experimental scheme.

Table N9. Experimental setup and data acquisition of combination A for the linear drive.

Row Num. / Experiment Num.	1	2	3	4	5	6	7	8	Results
	Frequency (Hz)	Amplitude (mm)	Amplitude coefficient	/	/	/	/	/	1-3: Q (nC)
1	0.6	8	1	/	/	/	/	/	17
2	0.6	12	2	/	/	/	/	/	31
3	0.6	16	3	/	/	/	/	/	589
4	0.6	20	4	/	/	/	/	/	1,242

Table Continued.

Row Num. / Experiment Num.	1	2	3	4	5	6	7	8	Results
	Frequency (Hz)	Amplitude (mm)	Amplitude coefficient	/	/	/	/	/	1-3: Q (nC)
5	0.6	24	5	/	/	/	/	/	1,107
6	0.6	28	6	/	/	/	/	/	1,945
7	0.6	32	7	/	/	/	/	/	2,075
8	0.8	8	2	/	/	/	/	/	144
9	0.8	12	3	/	/	/	/	/	325
10	0.8	16	4	/	/	/	/	/	2,073
11	0.8	20	5	/	/	/	/	/	1,827
12	0.8	24	6	/	/	/	/	/	1,652
13	0.8	28	7	/	/	/	/	/	2,140
14	0.8	32	1	/	/	/	/	/	380
15	1	8	3	/	/	/	/	/	940
16	1	12	4	/	/	/	/	/	2,092
17	1	16	5	/	/	/	/	/	2,061
18	1	20	6	/	/	/	/	/	2,110
19	1	24	7	/	/	/	/	/	2,187
20	1	28	1	/	/	/	/	/	1,314
21	1	32	2	/	/	/	/	/	1,874
22	1.2	8	4	/	/	/	/	/	1,957
23	1.2	12	5	/	/	/	/	/	1,990
24	1.2	16	6	/	/	/	/	/	2,067
25	1.2	20	7	/	/	/	/	/	2,427
26	1.2	24	1	/	/	/	/	/	1,942
27	1.2	28	2	/	/	/	/	/	2,347
28	1.2	32	3	/	/	/	/	/	2,267
29	1.4	8	5	/	/	/	/	/	2,330
30	1.4	12	6	/	/	/	/	/	2,422
31	1.4	16	7	/	/	/	/	/	2,432
32	1.4	20	1	/	/	/	/	/	2,359
33	1.4	24	2	/	/	/	/	/	2,331
34	1.4	28	3	/	/	/	/	/	2,403
35	1.4	32	4	/	/	/	/	/	2,425
36	1.6	8	6	/	/	/	/	/	2,326
37	1.6	12	7	/	/	/	/	/	2,445
38	1.6	16	1	/	/	/	/	/	113
39	1.6	20	2	/	/	/	/	/	2,361
40	1.6	24	3	/	/	/	/	/	2,283
41	1.6	28	4	/	/	/	/	/	2,416
42	1.6	32	5	/	/	/	/	/	2,469
43	1.8	8	7	/	/	/	/	/	2,372
44	1.8	12	1	/	/	/	/	/	111
45	1.8	16	2	/	/	/	/	/	2,412
46	1.8	20	3	/	/	/	/	/	2,432
47	1.8	24	4	/	/	/	/	/	2,379
48	1.8	28	5	/	/	/	/	/	2266
49	1.8	32	6	/	/	/	/	/	2193

5. The Calculation Method of the Range Analysis in Orthogonal Experimental Design (The method is the same as in Experiment 1.)

Table N10. Data analysis of combination A for the linear drive.

Row Num. / Experiment Num.	1	2	3	4	5	6	7	8	Results
	Frequency (Hz)	Amplitude (mm)	Amplitude coefficient	/	/	/	/	/	1-3: Q (nC)
y_{j1}	7,006	10,086	6,237	/	/	/	/	/	/
y_{j2}	8,540	9,416	11,500	/	/	/	/	/	/
y_{j3}	12,578	11,747	11,238	/	/	/	/	/	/
y_{j4}	14,998	14,758	14,584	/	/	/	/	/	/
y_{j5}	16,702	13,881	14,050	/	/	/	/	/	/
y_{j6}	14,413	14,831	14,714	/	/	/	/	/	/
y_{j7}	14,165	13,683	16,078	/	/	/	/	/	/
$\overline{y}_{j1}$	1,001	1,441	891	/	/	/	/	/	/
$\overline{y}_{j2}$	1,220	1,345	1,643	/	/	/	/	/	/
$\overline{y}_{j3}$	1,797	1,678	1,605	/	/	/	/	/	/
$\overline{y}_{j4}$	2,143	2,108	2,083	/	/	/	/	/	/
$\overline{y}_{j5}$	2,386	1,983	2,007	/	/	/	/	/	/
$\overline{y}_{j6}$	2,059	2,119	2,102	/	/	/	/	/	/
$\overline{y}_{j7}$	2,024	1,955	2,297	/	/	/	/	/	/
R_j	2,386	2,108	2,083	/	/	/	/	/	/
Trend analysis chart	Figure N3a.	Figure N3b.	Figure N3c.	/	/	/	/	/	/
Optimal combination	1.4	20	4	/	/	/	/	/	/
Primary and secondary factors	Frequency ＞	Amplitude ＞	Amplitude coefficient	/	/	/	/	/	/

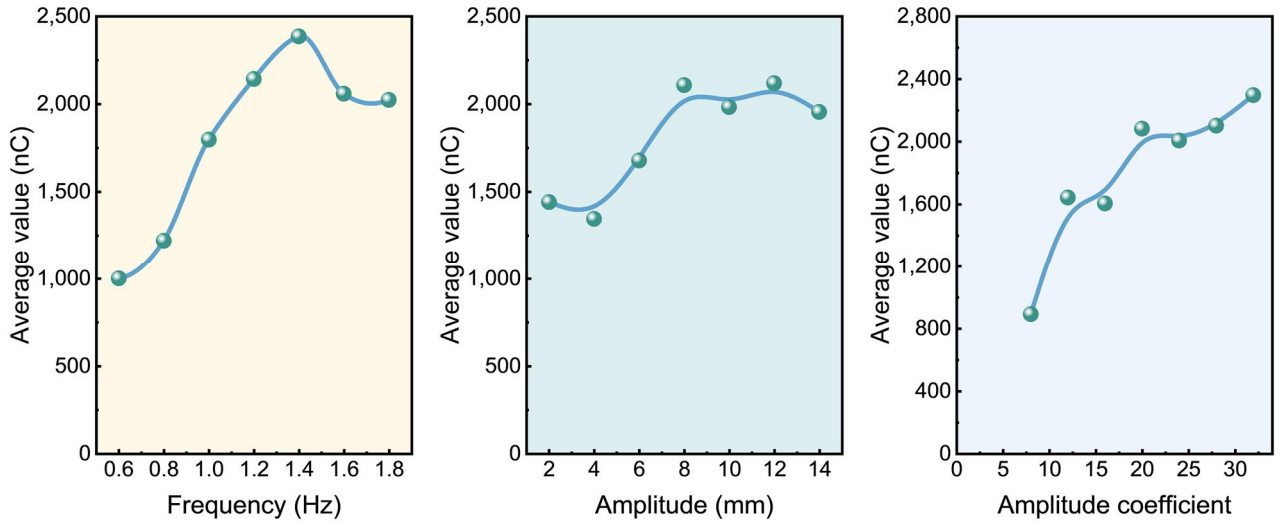

Figure N3. The output variation trend of RD-TENG is based on the frequency-reducing and amplitude-amplifying magnetic repulsion pendulum under a six-degree-of-freedom platform linear drive concerning each input parameter.

Table N11. Experimental setup and data acquisition of combination B for the swinging drive.

Row Num. / Experiment Num	1	2	3	5	6	7	8	Results
	Frequency (Hz)	Pendulum angle (°)	Amplitude coefficient	/	/	/	/	1-3: Q (nC)
1	0.6	2	1	/	/	/	/	362
2	0.6	4	1.5	/	/	/	/	1,386
3	0.6	6	2	/	/	/	/	1,793
4	0.6	8	2.5	/	/	/	/	1,892
5	0.6	10	3	/	/	/	/	2,043
6	0.6	12	3.5	/	/	/	/	2,216
7	0.6	14	4	/	/	/	/	2,160
8	0.8	6	1.5	/	/	/	/	1,922
9	0.8	8	2	/	/	/	/	1,945
10	0.8	10	2.5	/	/	/	/	1,927
11	0.8	12	3	/	/	/	/	1,910
12	0.8	14	3.5	/	/	/	/	1,966
13	0.8	2	4	/	/	/	/	2,003
14	0.8	4	1	/	/	/	/	1,786
15	1	10	2	/	/	/	/	1,862
16	1	12	2.5	/	/	/	/	1,689
17	1	14	3	/	/	/	/	1,928
18	1	2	3.5	/	/	/	/	1,890
19	1	4	4	/	/	/	/	2,020
20	1	6	1	/	/	/	/	1,725
21	1	8	1.5	/	/	/	/	1,998
22	1.2	14	2.5	/	/	/	/	1,961
23	1.2	2	3	/	/	/	/	2,016
24	1.2	4	3.5	/	/	/	/	2,084
25	1.2	6	4	/	/	/	/	1,925
26	1.2	8	1	/	/	/	/	2,038
27	1.2	10	1.5	/	/	/	/	2,097
28	1.2	12	2	/	/	/	/	2,014
29	1.4	4	3	/	/	/	/	2,050
30	1.4	6	3.5	/	/	/	/	2,064
31	1.4	8	4	/	/	/	/	1,947
32	1.4	10	1	/	/	/	/	2,248
33	1.4	12	1.5	/	/	/	/	2,004
34	1.4	14	2	/	/	/	/	1,948
35	1.4	2	2.5	/	/	/	/	2,060
36	1.6	8	3.5	/	/	/	/	1,974
37	1.6	10	4	/	/	/	/	1,979
38	1.6	12	1	/	/	/	/	1,976
39	1.6	14	1.5	/	/	/	/	1,989
40	1.6	2	2	/	/	/	/	1,978
41	1.6	4	2.5	/	/	/	/	2,004
42	1.6	6	3	/	/	/	/	1,997
43	1.8	12	4	/	/	/	/	1,994
44	1.8	14	1	/	/	/	/	1,939
45	1.8	2	1.5	/	/	/	/	1,540
46	1.8	4	2	/	/	/	/	1,951

Table Continued.

Row Num. / Experiment Num	1	2	3	5	6	7	8	Results
	Frequency (Hz)	Pendulum angle (°)	Amplitude coefficient	/	/	/	/	1-3: Q (nC)
47	1.8	6	2.5	/	/	/	/	1,942
48	1.8	8	3	/	/	/	/	1,945
49	1.8	10	3.5	/	/	/	/	2,007

6. The Calculation Method of the Range Analysis in Orthogonal Experimental Design (The method is the same as in Experiment 1).

Table N12. Data analysis of combination B for the swinging drive.

Row Num. / Experiment Num	1	2	3	5	6	7	8	Results
	Frequency (Hz)	Pendulum angle (°)	Amplitude coefficient	/	/	/	/	1-3: Q (nC)
y_{j1}	11,852	11,849	12,074	/	/	/	/	/
y_{j2}	13,459	13,281	12,936	/	/	/	/	/
y_{j3}	13,112	13,368	13,491	/	/	/	/	/
y_{j4}	14,135	13,798	13,475	/	/	/	/	/
y_{j5}	14,321	14,163	13,889	/	/	/	/	/
y_{j6}	13,897	13,803	14,201	/	/	/	/	/
y_{j7}	13,318	13,891	14,028	/	/	/	/	/
$\overline{y}_{j1}$	1,693	1,693	1,725	/	/	/	/	/
$\overline{y}_{j2}$	1,923	1,897	1,848	/	/	/	/	/
$\overline{y}_{j3}$	1,873	1,910	1,927	/	/	/	/	/
$\overline{y}_{j4}$	2,019	1,971	1,925	/	/	/	/	/
$\overline{y}_{j5}$	2,046	2,023	1,984	/	/	/	/	/
$\overline{y}_{j6}$	1,985	1,972	2,029	/	/	/	/	/
$\overline{y}_{j7}$	1,903	1,984	2,004	/	/	/	/	/
R_j	2,046	242	1,925	/	/	/	/	/
Trend analysis chart	Figure N4a.	Figure N4b.	Figure N4c.	/	/	/	/	/
Optimal combination	1.4	10	4	/	/	/	/	/
Primary and secondary factors	Frequency ＞ Amplitude coefficient ＞ Pendulum angle			/	/	/	/	/

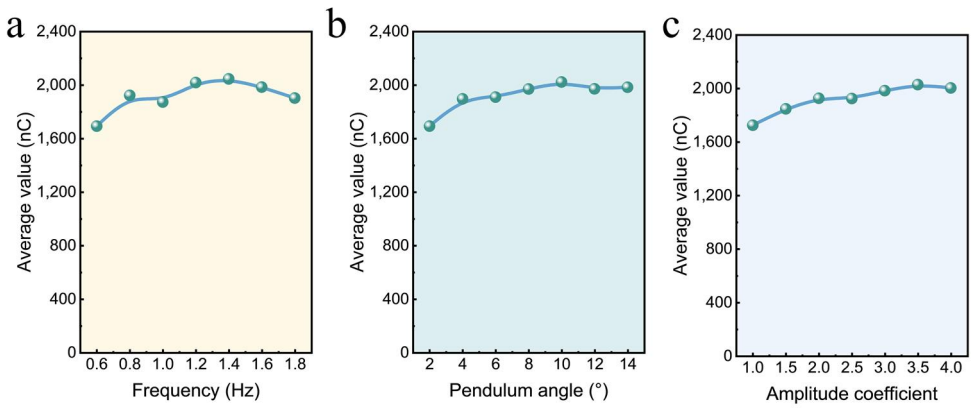

Figure N4. The output variation trend of RD-TENG is based on the frequency-reducing and amplitude-amplifying magnetic repulsion pendulum under a six-degree-of-freedom platform swinging drive concerning each input parameter.

7. Conclusion

Combination A investigates the optimal combination and system's best output of the RD-TENG under linear drive based on the frequency-reducing and amplitude-amplifying magnetic repulsion pendulum, considering the relevant input parameters — frequency, amplitude, and amplitude coefficient — across the six degrees of freedom. Combination B explores the optimal combination and system's optimal output of the RD-TENG under swinging drive, focusing on the relevant excitation output parameters — frequency, angle, and amplitude coefficient — across the six degrees of freedom. The final result indicates that under linear drive, the system achieves optimal output with frequency, amplitude, and amplitude coefficient set to 1.4 Hz, 20 mm, and 4, respectively, with the hierarchical influence relationship being: frequency > amplitude > amplitude coefficient. For swinging drive, the optimal combination is: frequency 1.4 Hz, angle 10°, and amplitude coefficient 4, with the impact hierarchy being: angle > frequency > amplitude coefficient. From the trend chart, it can be concluded that under linear driving, all driving parameters collectively influence the results. After eliminating error factors, amplitude, and amplitude coefficient have a relatively smaller impact, while frequency is the primary influencing factor. This indicates that the frequency-reducing and amplitude-amplifying magnetic repulsion pendulum inherently amplifies the small external driving amplitude into a larger working amplitude for the RD-TENG. In the swinging drive mode, individual parameters have little effect on the outcome. As long as the external input meets the system's minimum triggering condition, the RD-TENG system can operate efficiently. This demonstrates the frequency-reducing and amplitude-amplifying magnetic repulsion pendulum's significant potential in reducing response frequency and increasing working amplitude.

Supplementary Figures

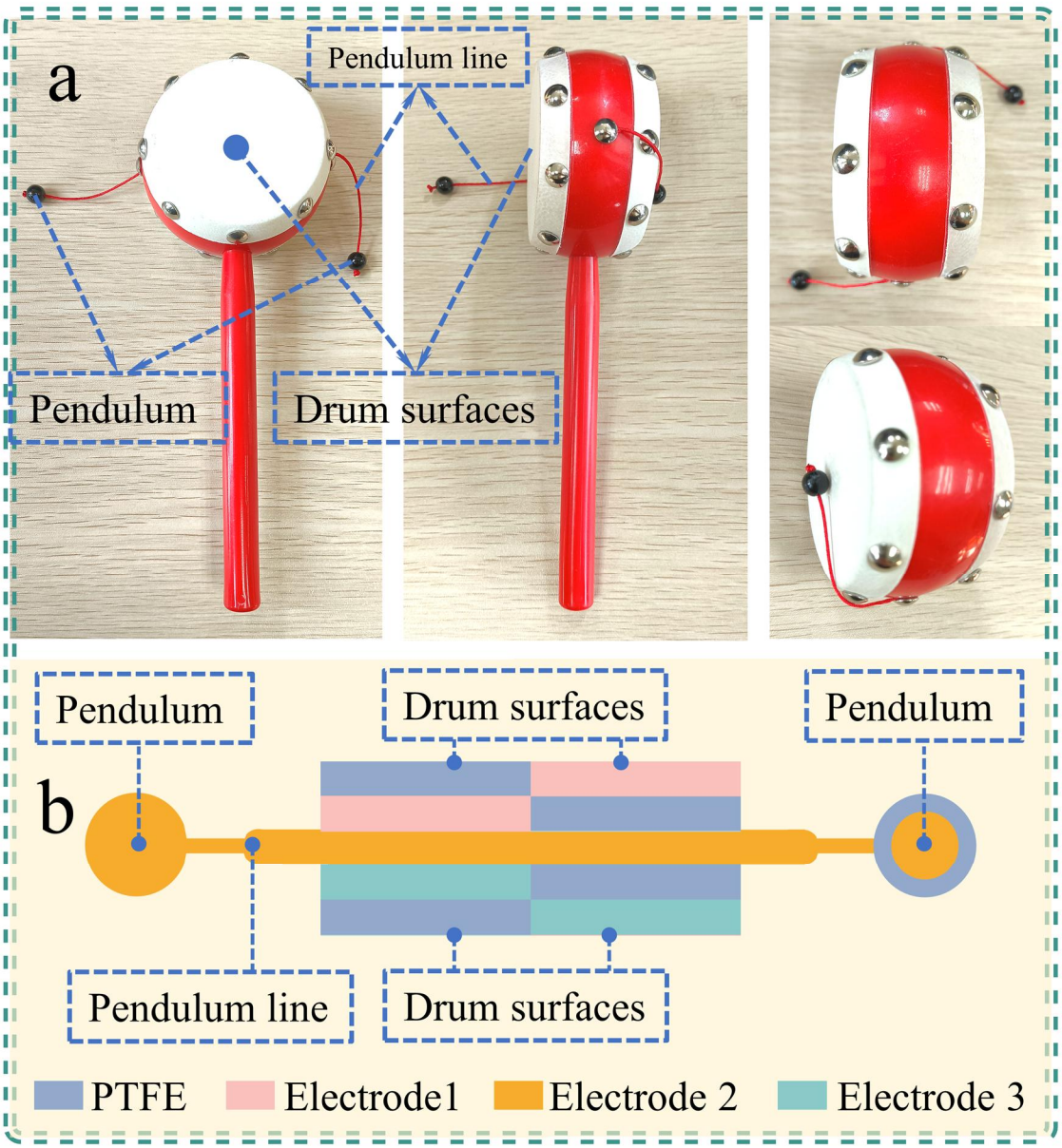

Fig. S1. (a) Photograph of the rattle-drum. (b) rattle-drum-type TENG

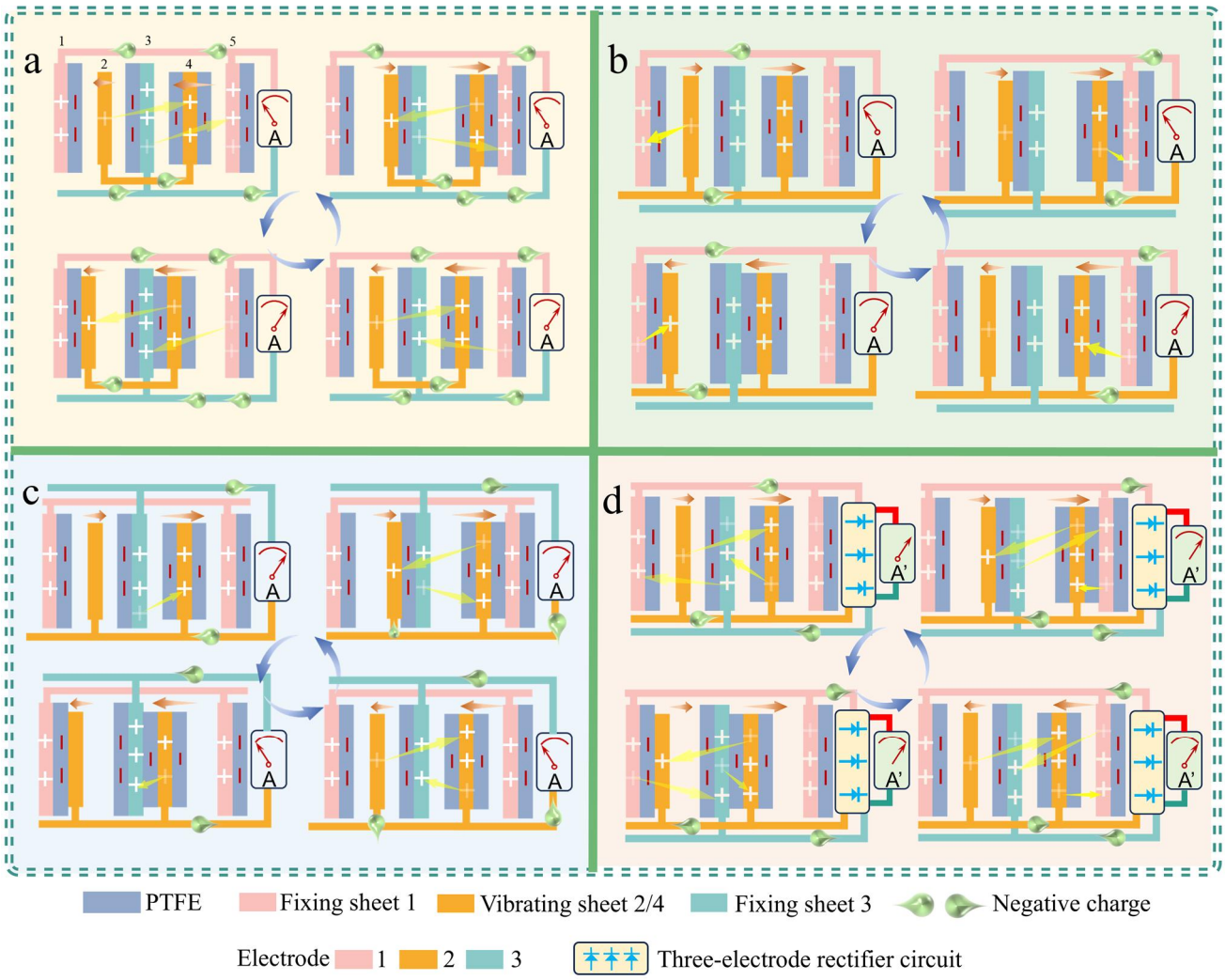

Fig. S2. Charge dispatch and transfer schematic diagram for each electrode pair of RD-TENG. (a) 1-3 electrode pair. (b) 1-2 electrode pair. (c) 2-3 electrode pair. (d) rectified electrode pair.

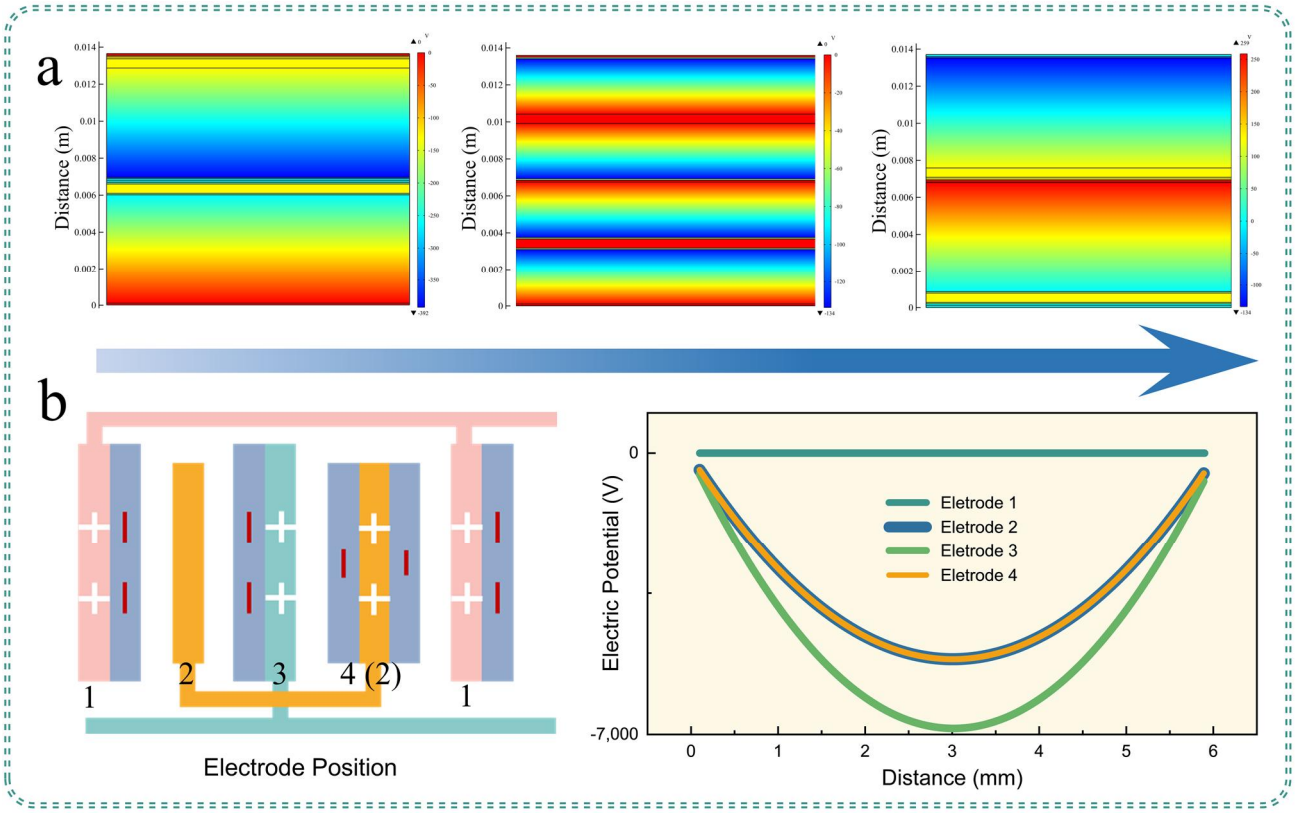

Fig. S3. (a) Simulation of the electric potential of the vibrating sheet moving from one end to the other in the RD-TENG. (b) Positions of each electrode and their electric potential variation curves as the vibrating sheet oscillates from one end to the other.

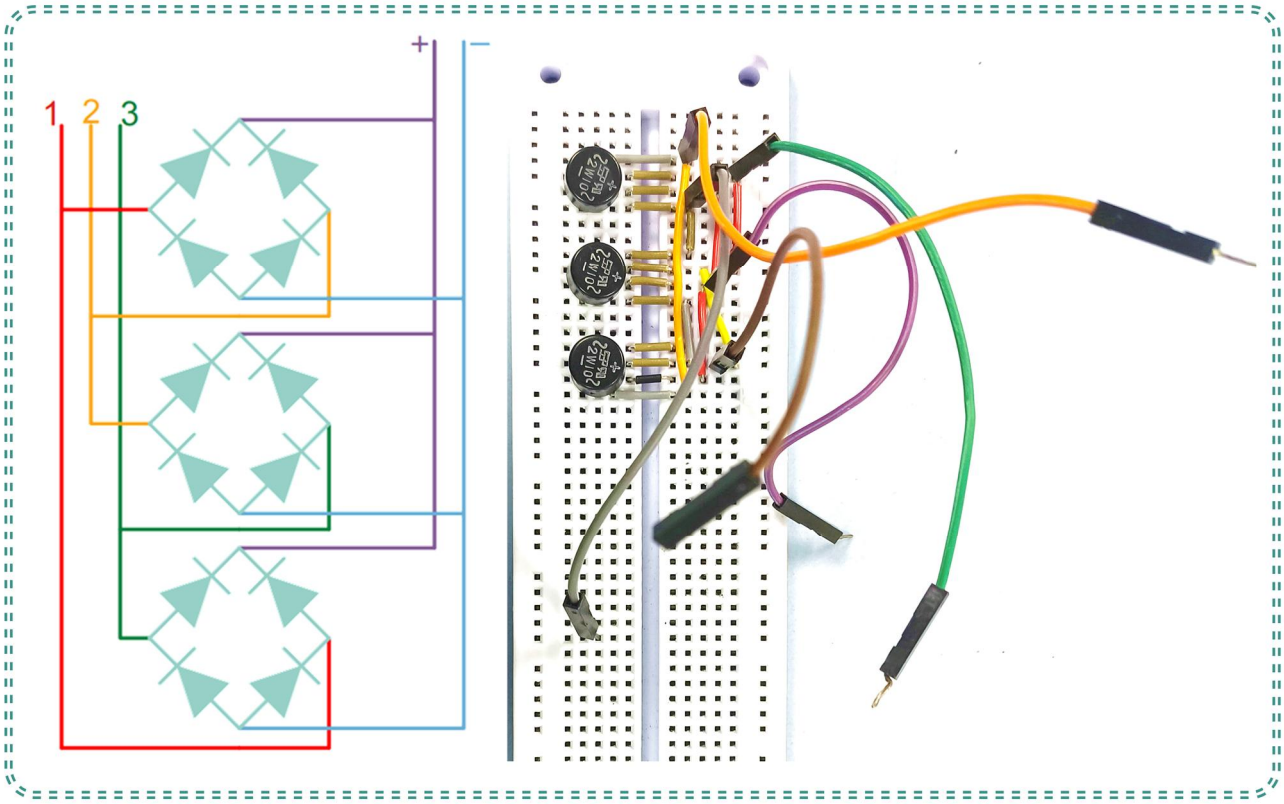

Fig. S4. Three-electrode rectifier circuit diagram and its physical circuit image.

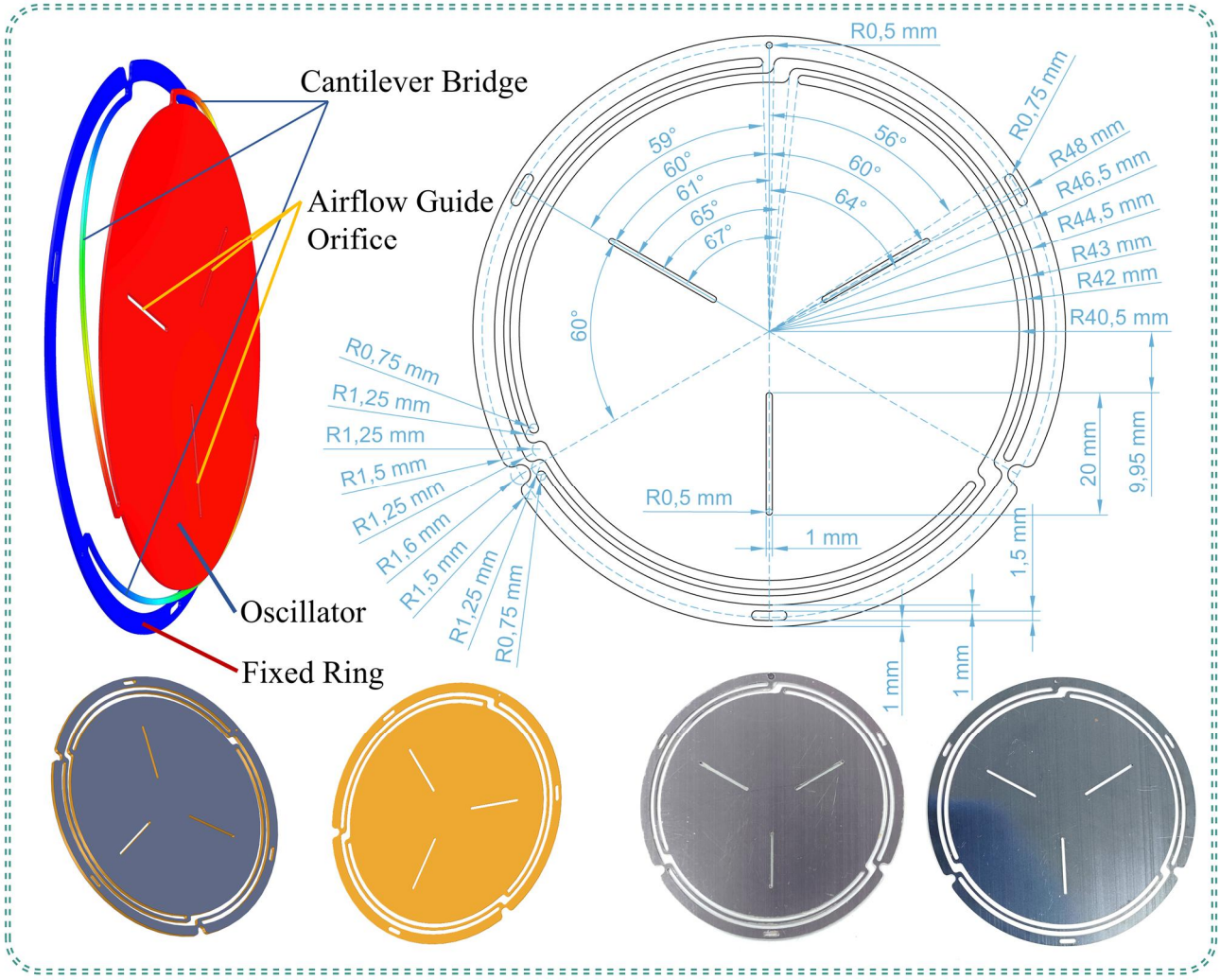

Fig. S5. Vibrating sheet style, parameters, model, and physical image.

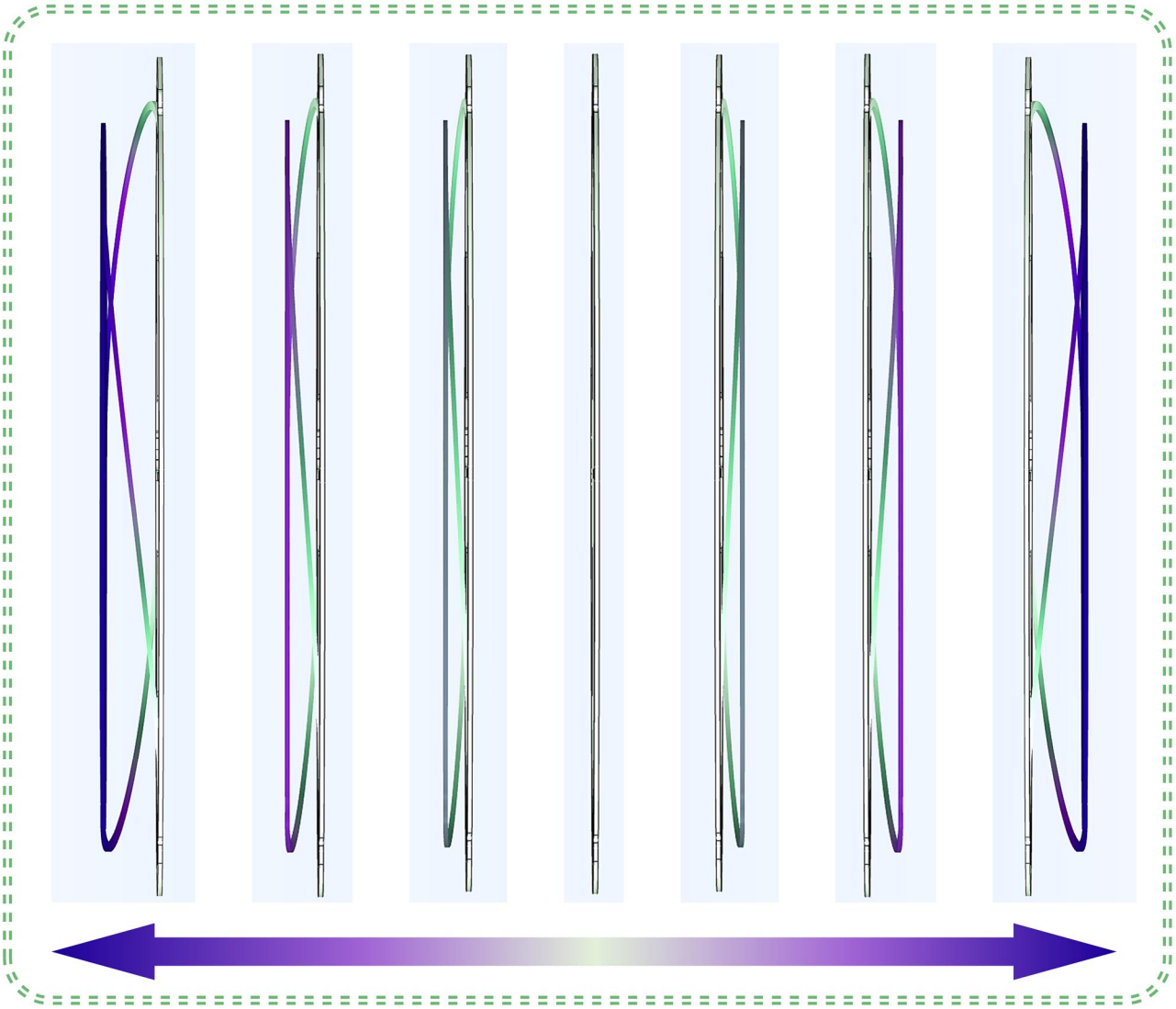

Fig. S6. Vibration simulation of the vibrating steel sheet.

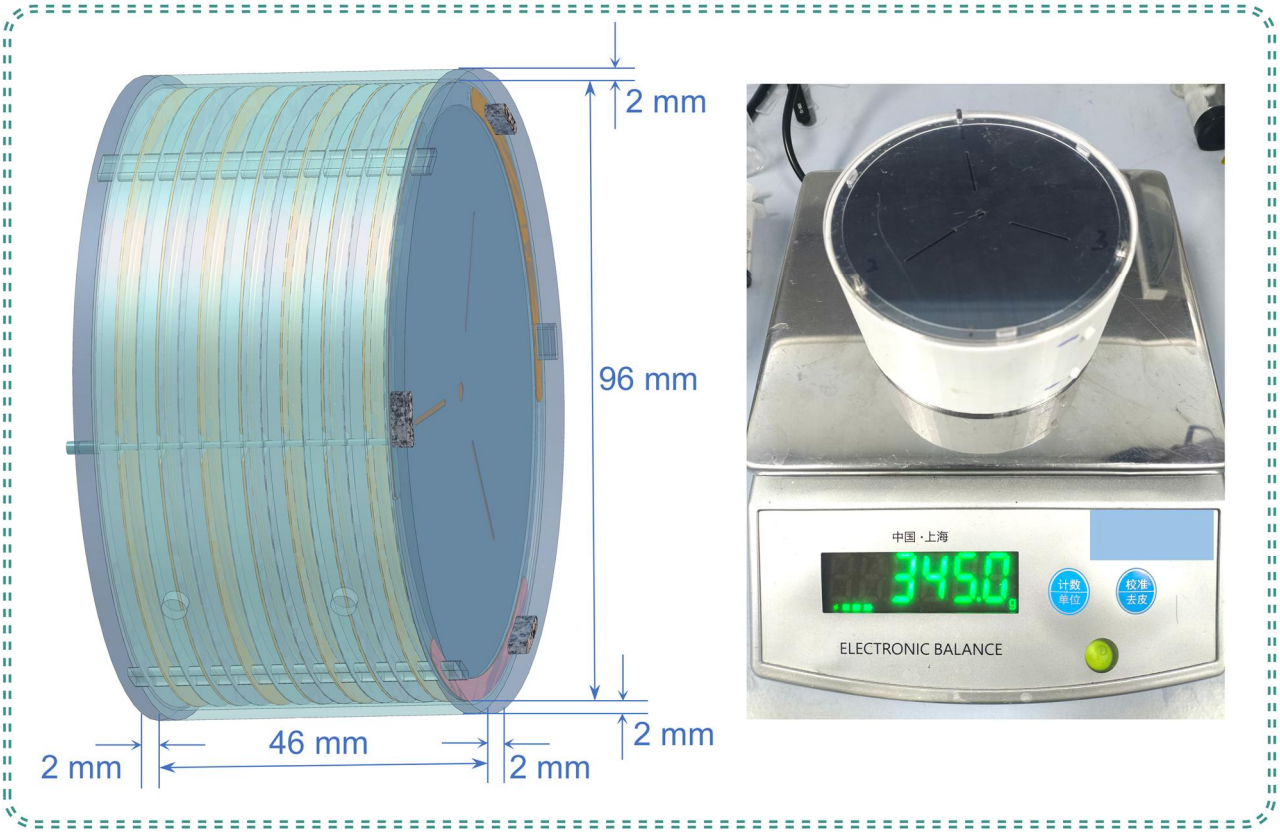

Fig. S7. Packaged device model parameters and physical image.

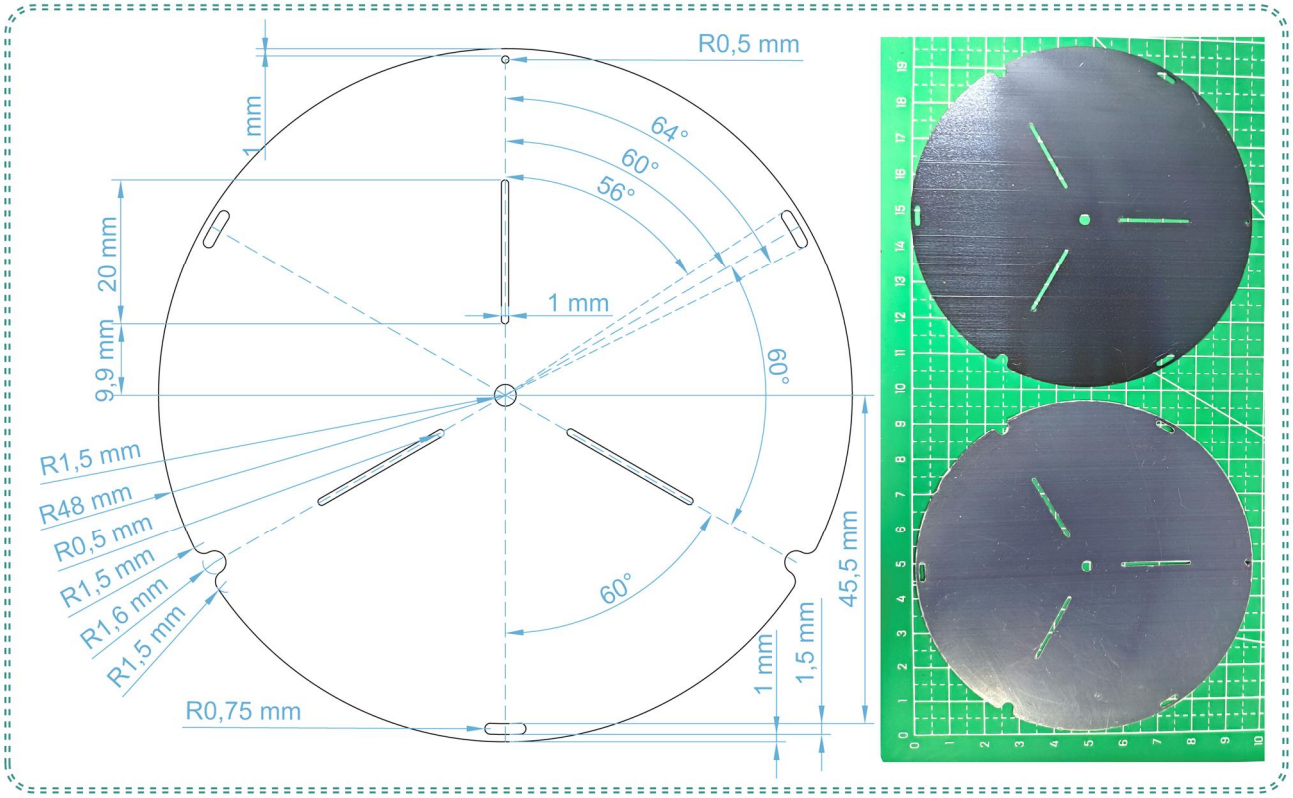

Fig. S8. Fixing sheet parameters and physical image.

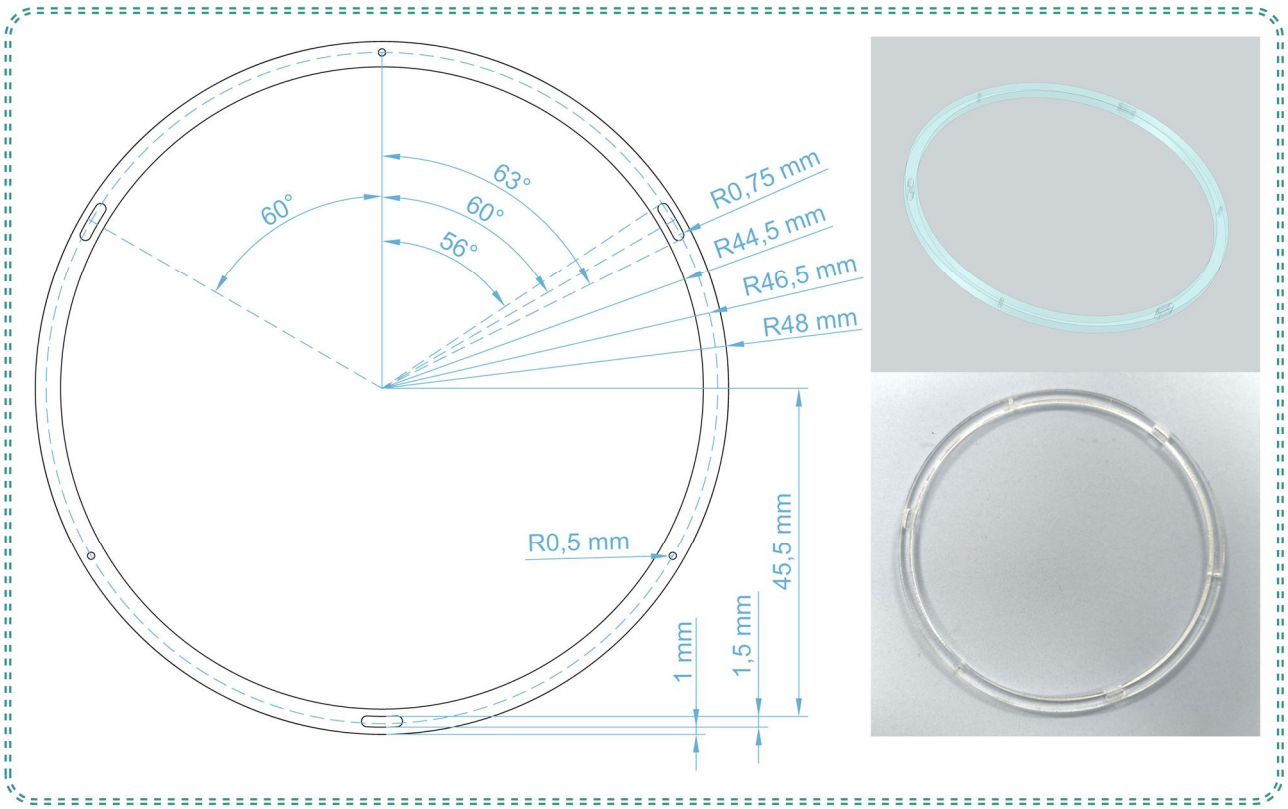

Fig. S9. Acrylic ring gasket parameters, model, and physical image.

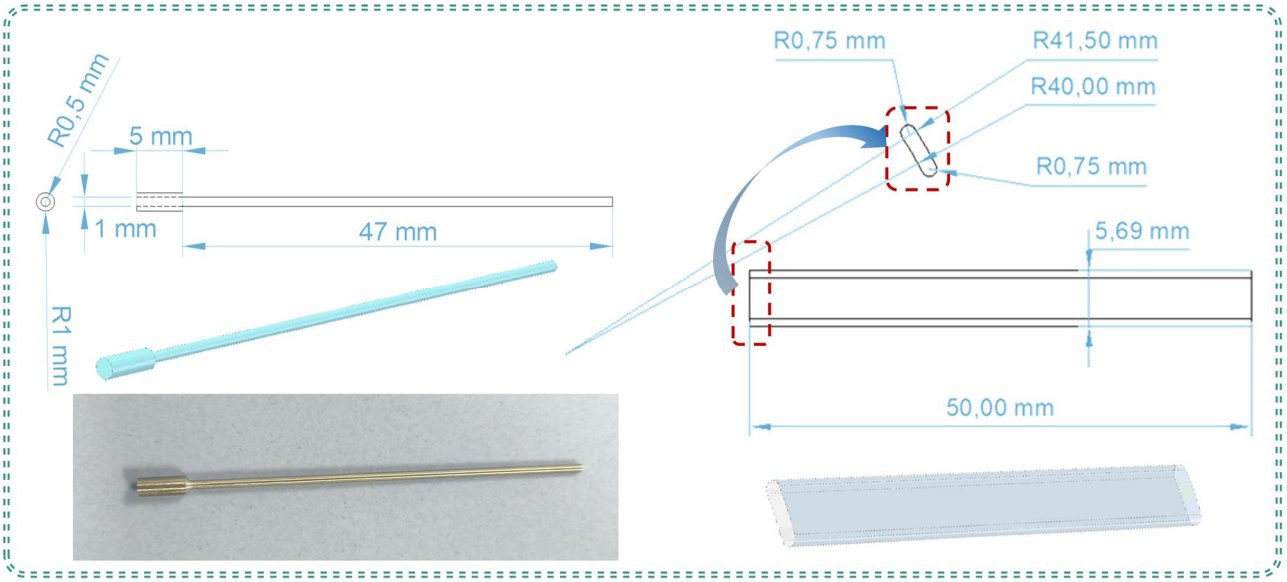

Fig. S10. Push pin and latch parameters.

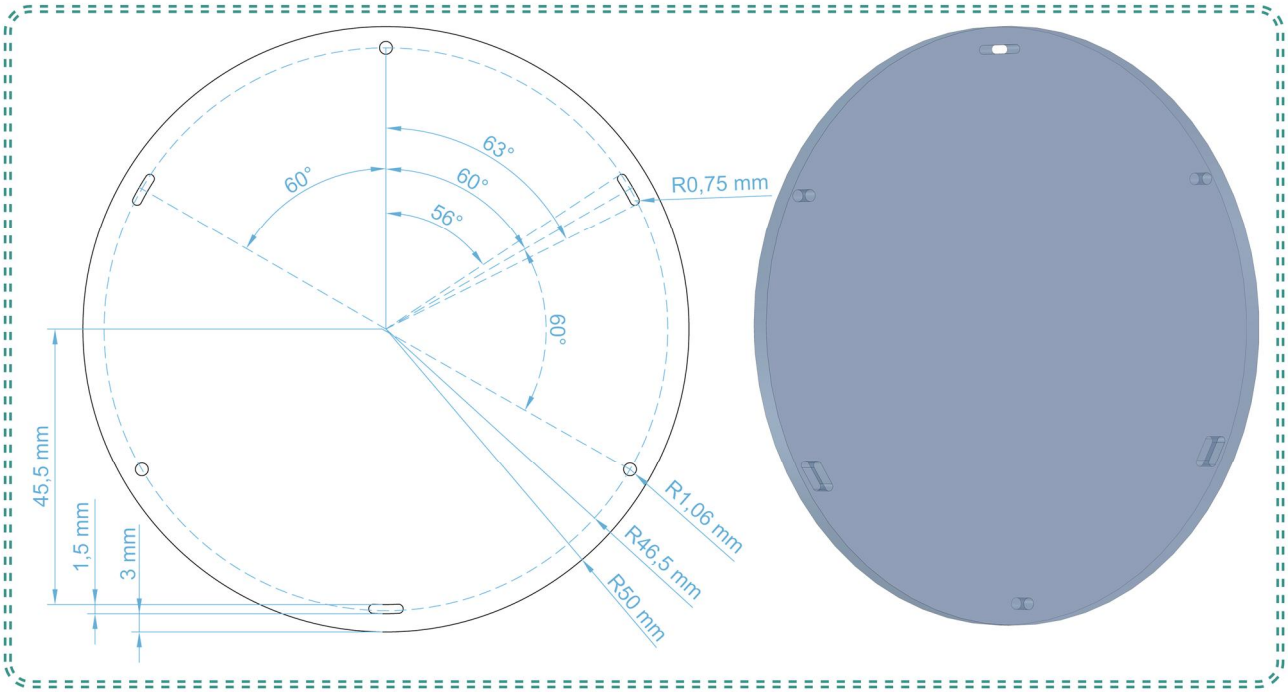

Fig. S11. Bottom sealing plate and its parameters.

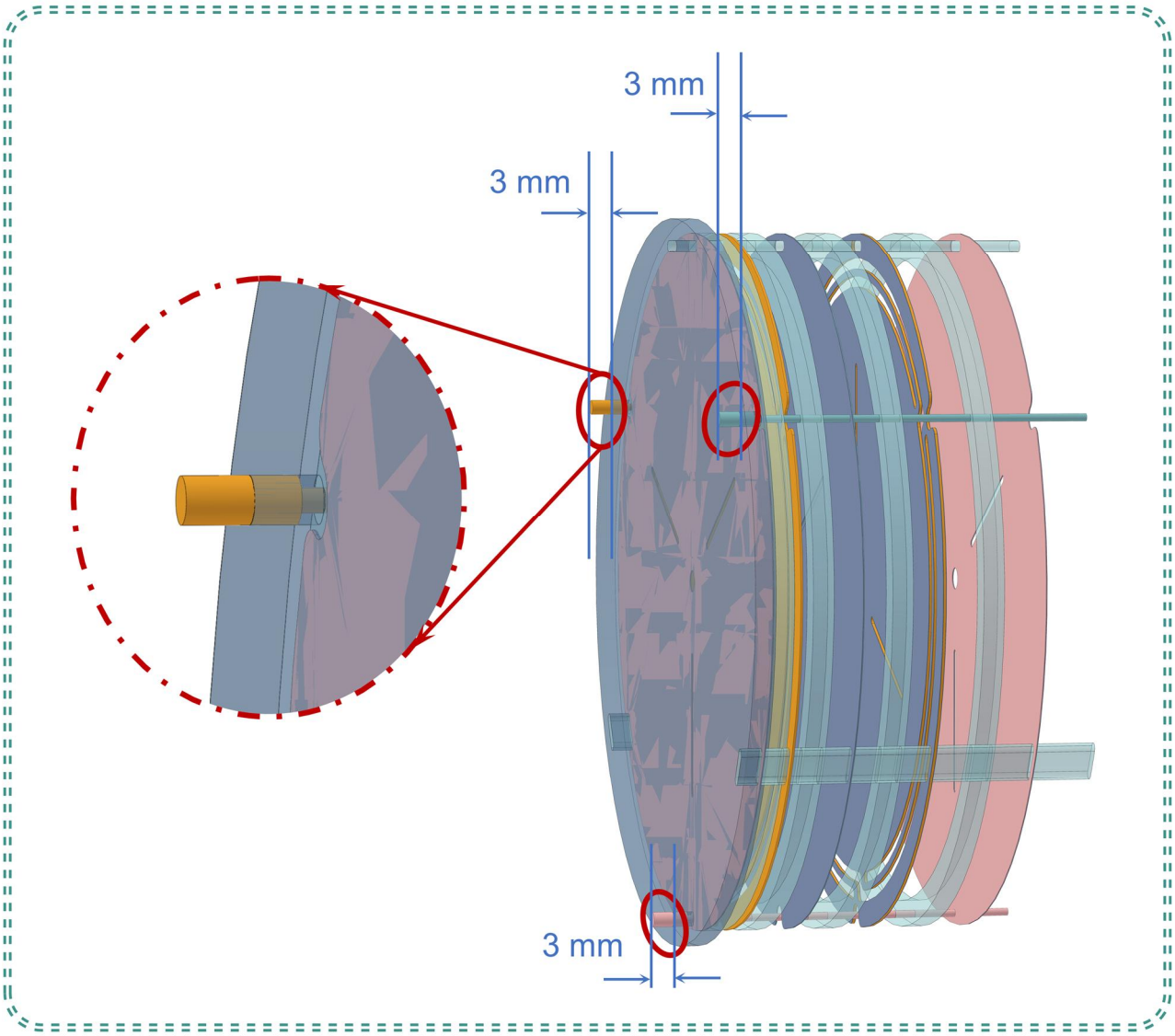

Fig. S12. The protruding end of the push pin serves as the electrode lead-out terminal.

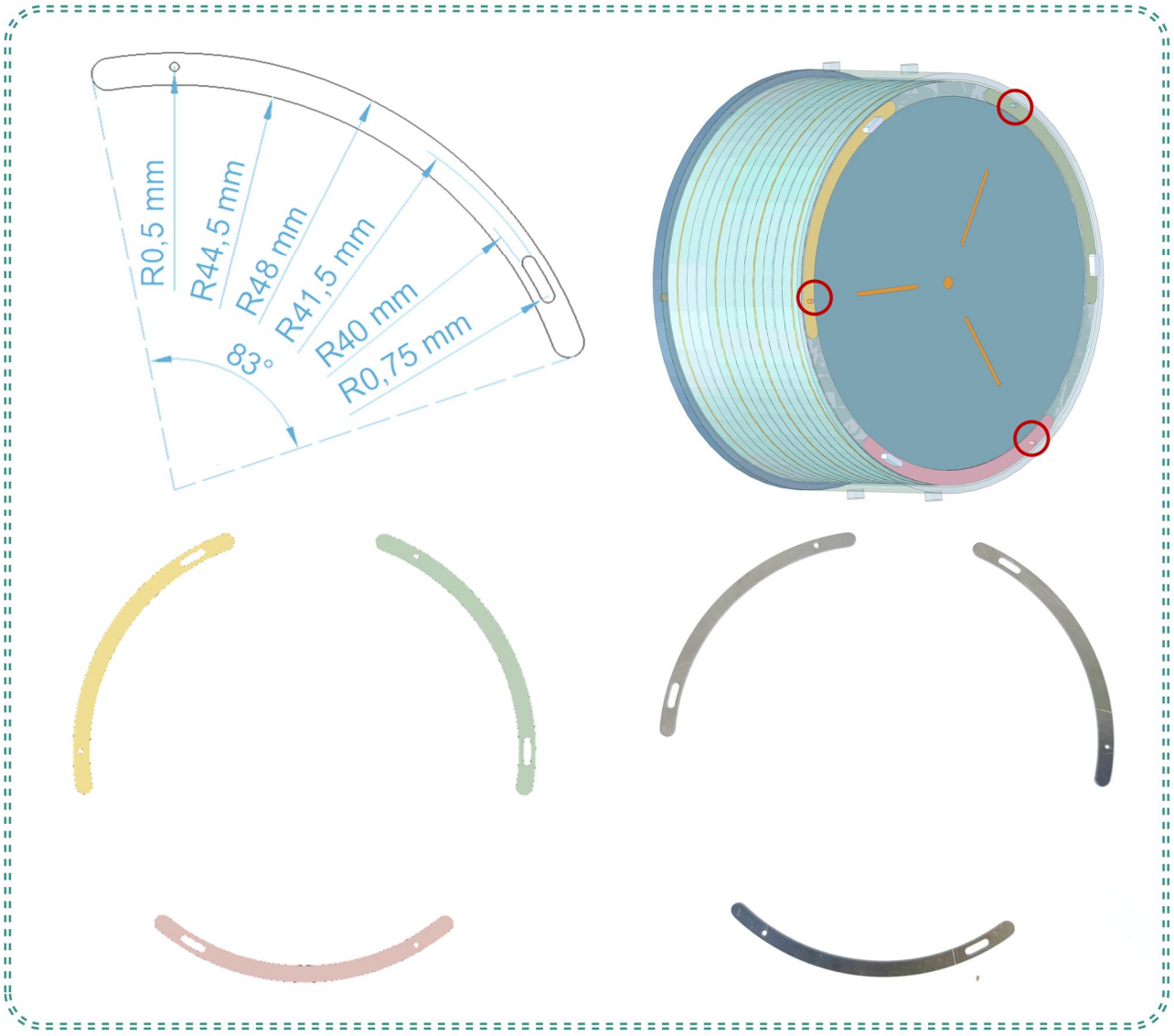

Fig. S13. Electrode conductive sheet parameters, position, model, and physical image.

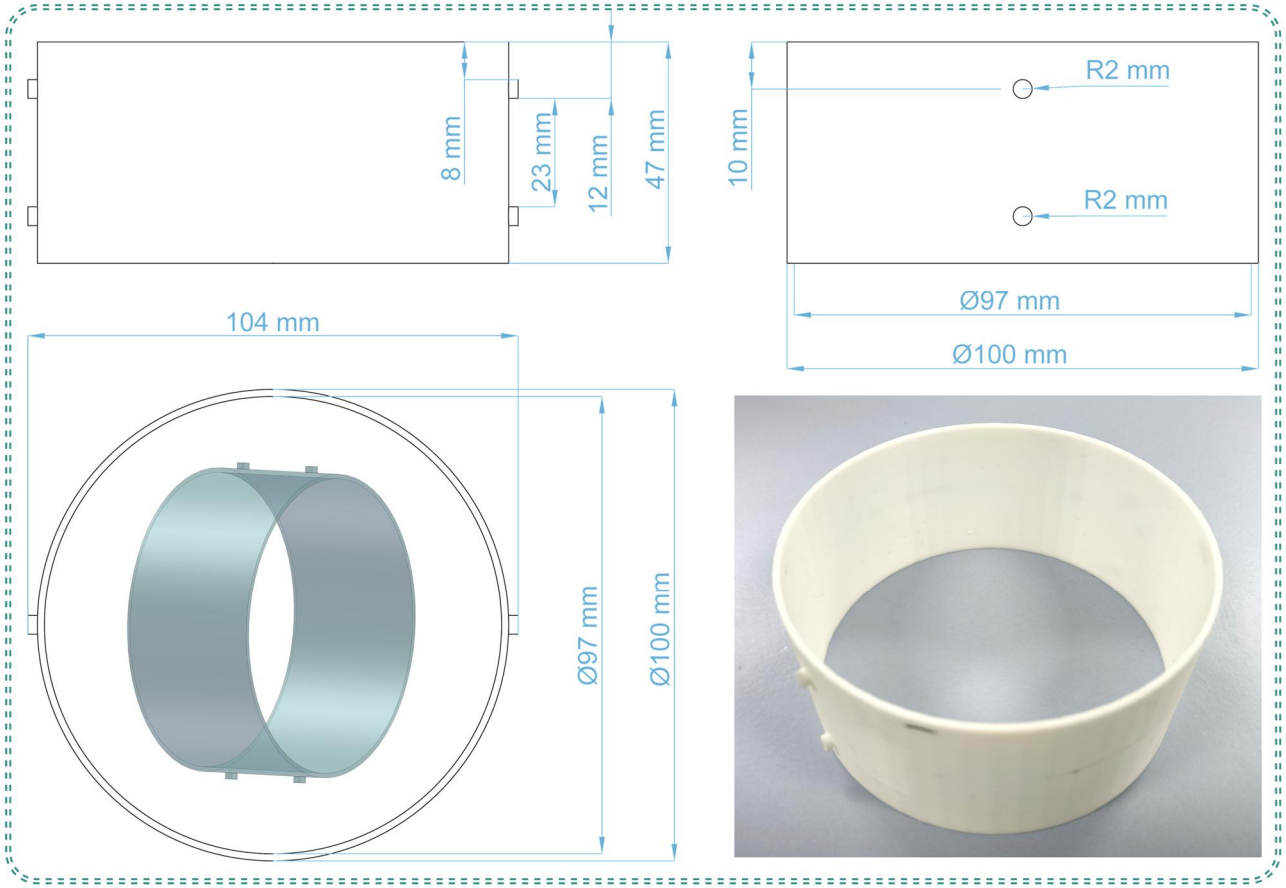

Fig. S14. Packaging barrel parameters and its physical image.

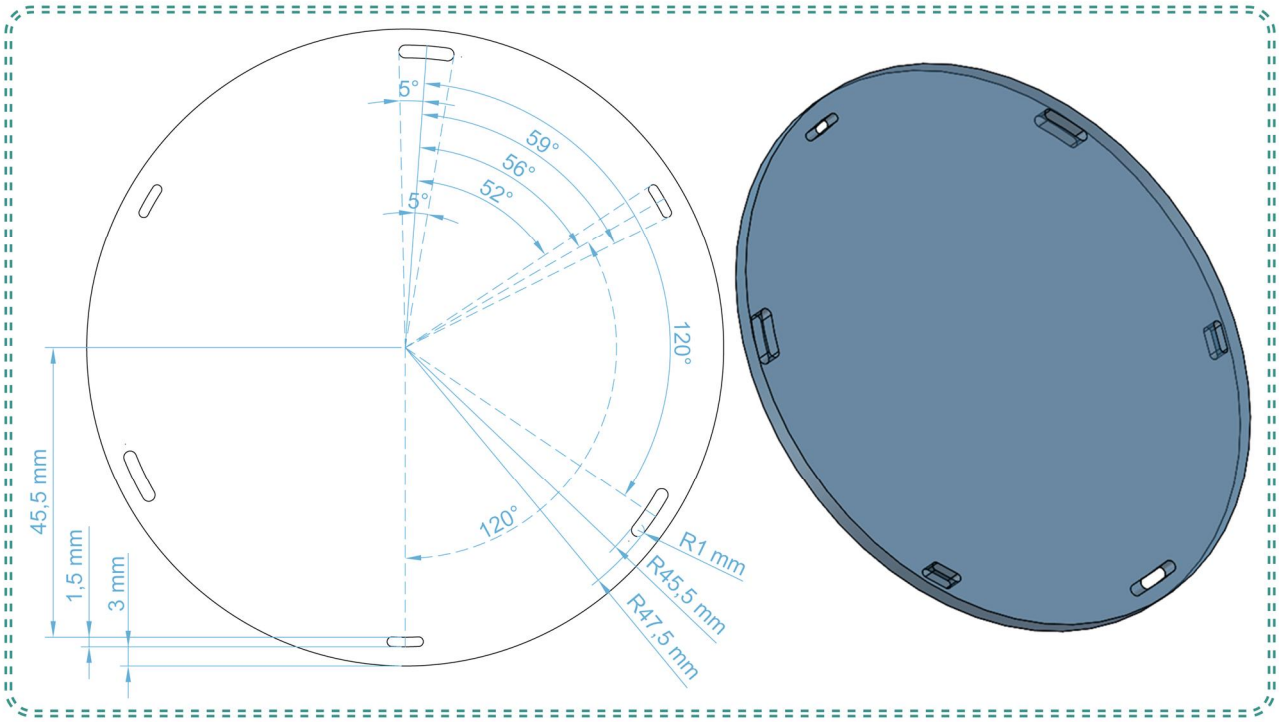

Fig. S15. Top sealing plate and its parameters.

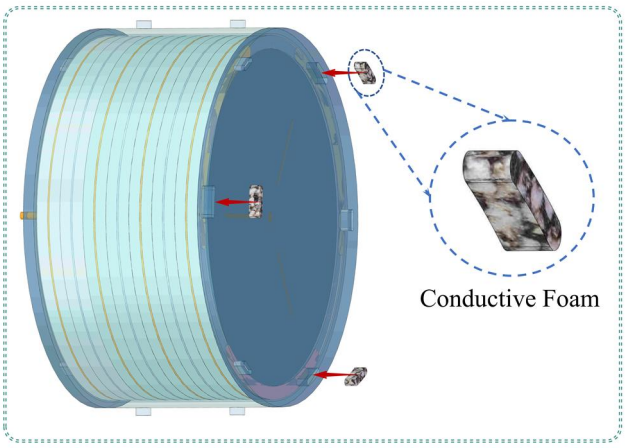

Fig. S16. Conductive sponge and its installation location.

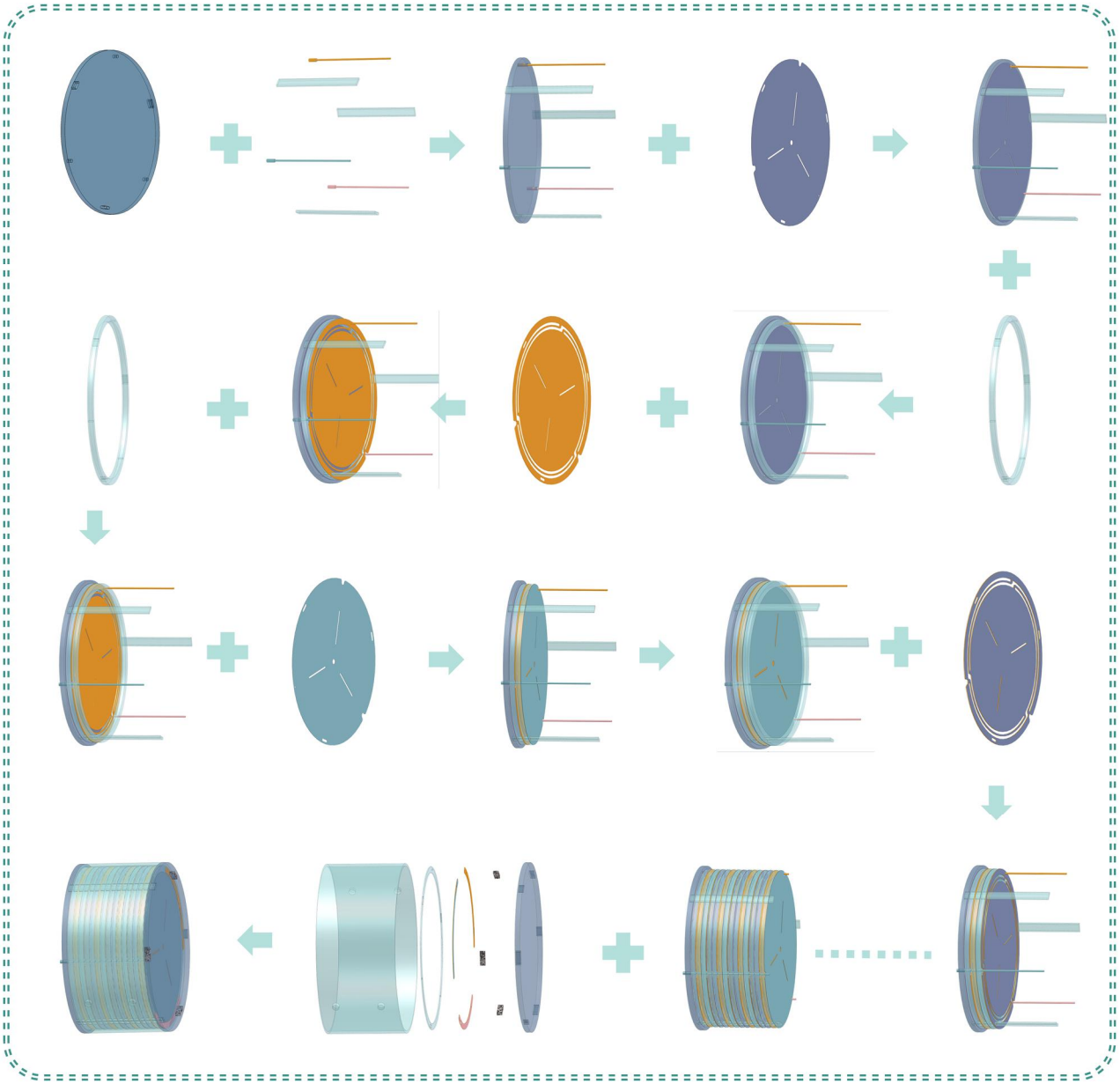

Fig. S17. Assembly steps of the RD-TENG device.

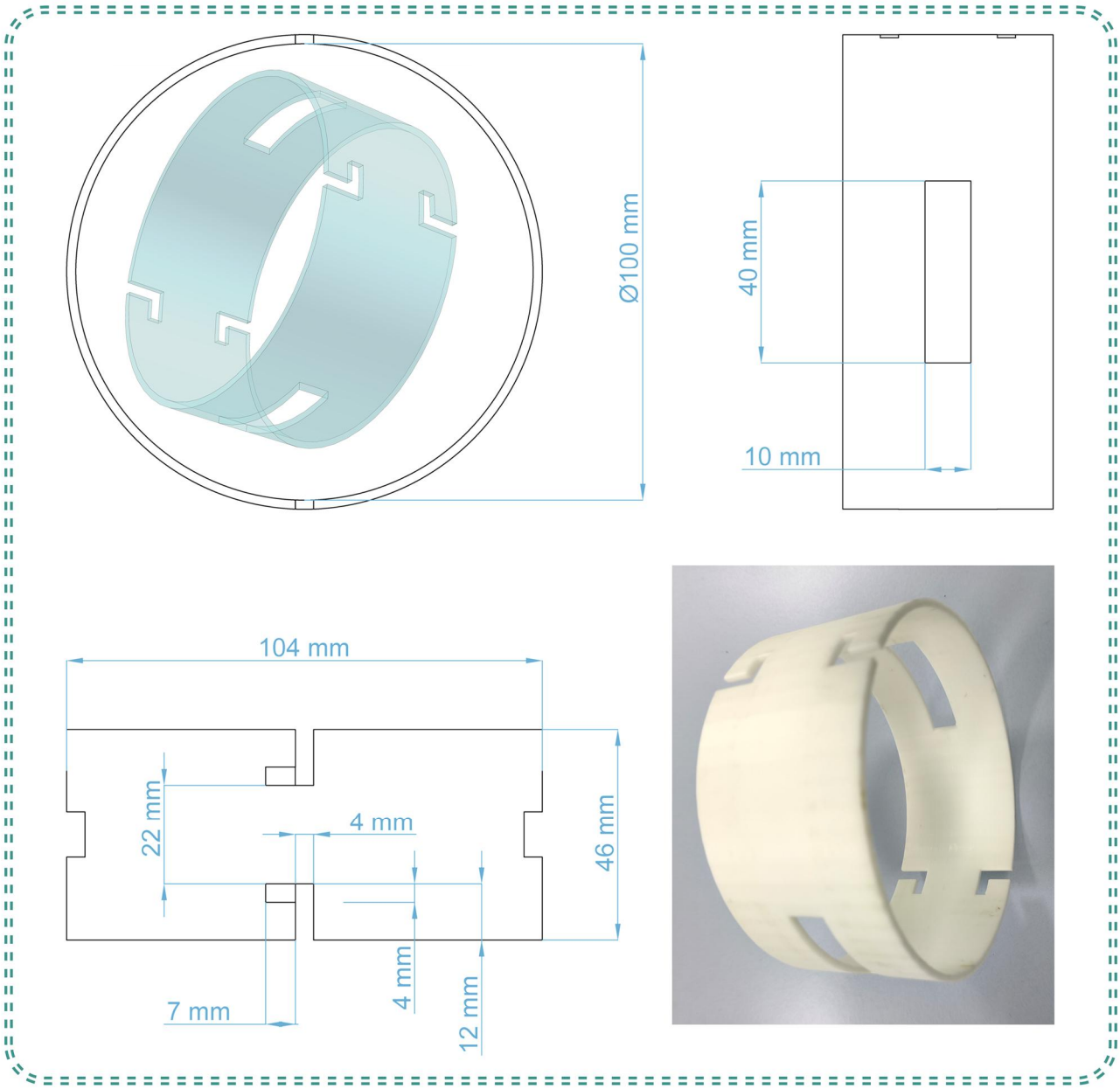

Fig. S18. Parameters and physical image of the rotating-clasp device.

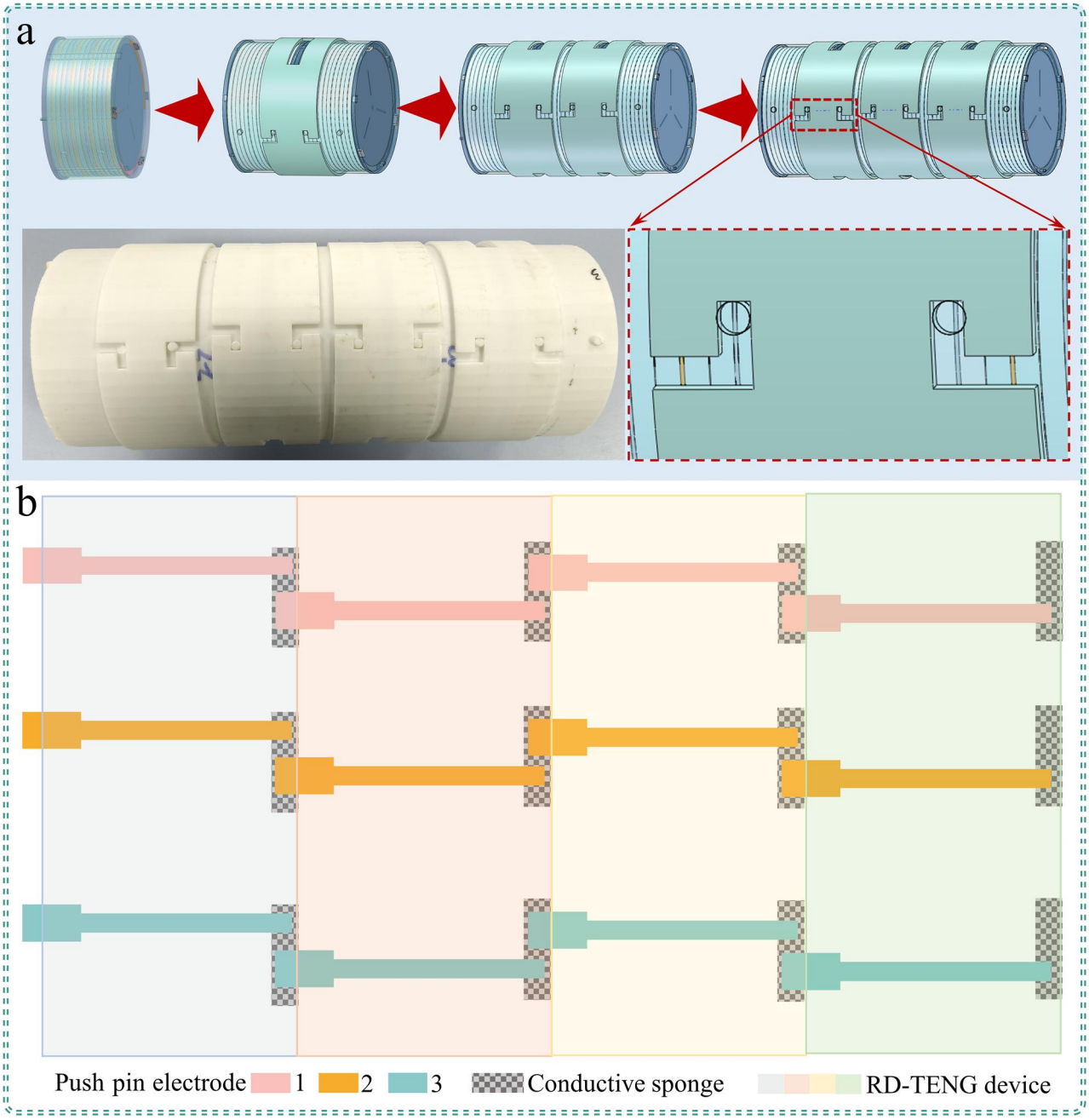

Fig. S19. (a) Details and physical image of the RD-TENG device array. (b) Connection method of push-pin electrodes in the device array.

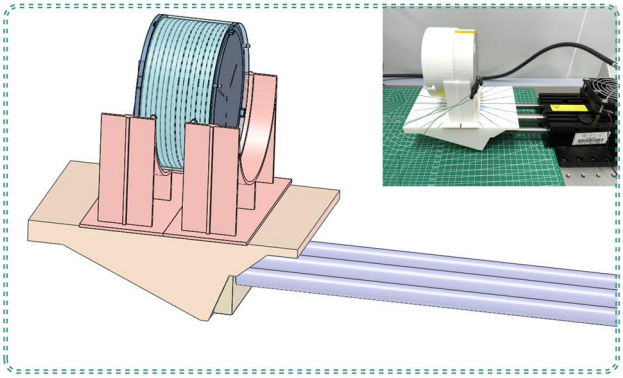

Fig. S20. Vibrational energy simulation testing platform.

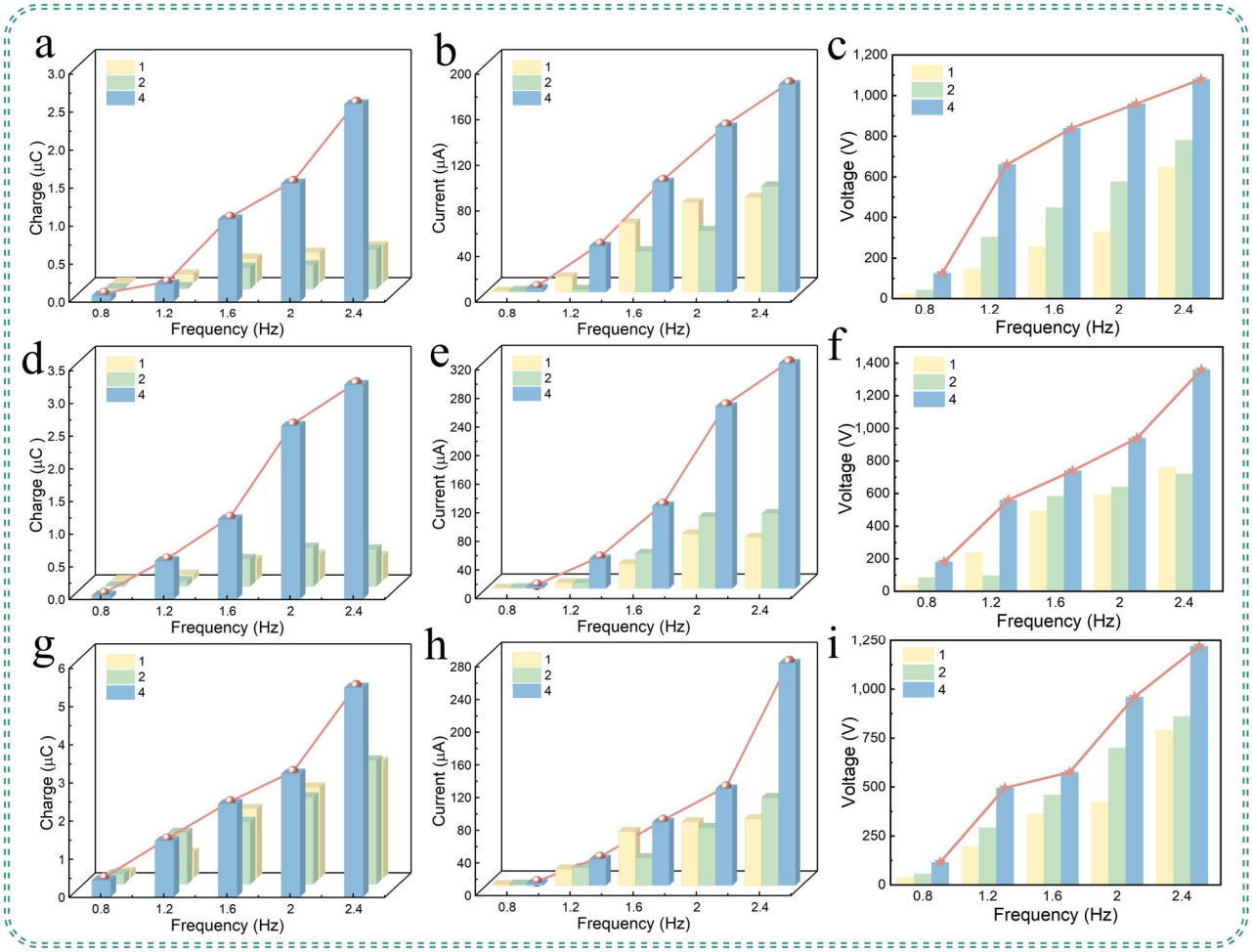

Fig. S21. Comparison of the output of RD-TENG (Structure 4) with traditional structures. (a-c) Comparison of output charge, current, and voltage for the 1-2 electrode pair across different structures. (d-f) Comparison of output charge, current, and voltage for the 2-3 electrode pair across different structures. (g-h) Comparison of output charge, current, and voltage for the rectified electrode pair across different structures.

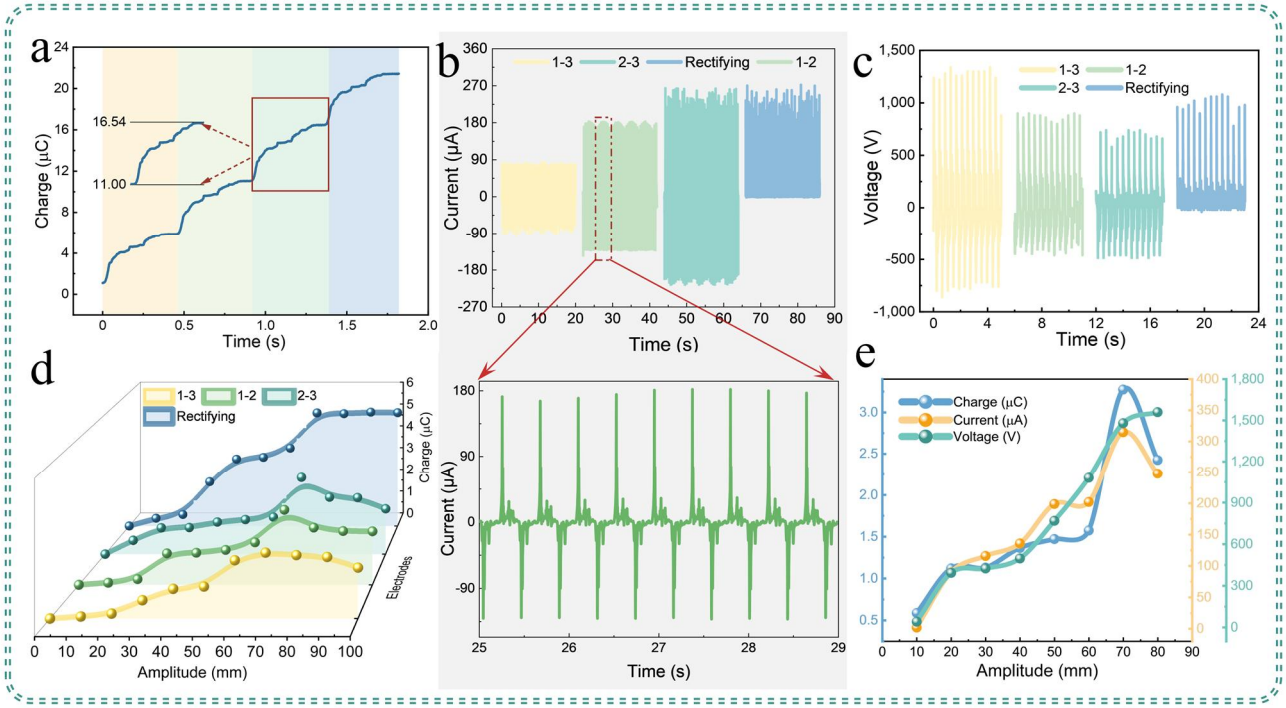

Fig. S22. Output characteristics of RD-TENG. (a) Cumulative charge of the rectified electrode pair of RD-TENG under optimal excitation conditions. (b-c) Short-circuit current and open-circuit voltage of each electrode pair. (d) The relationship between the charge output of each electrode pair and amplitude under a frequency of 2.4 Hz. (e) The output relationship between the output quantities of the 2-3 electrode pair and the amplitude under a frequency of 2.4 Hz.

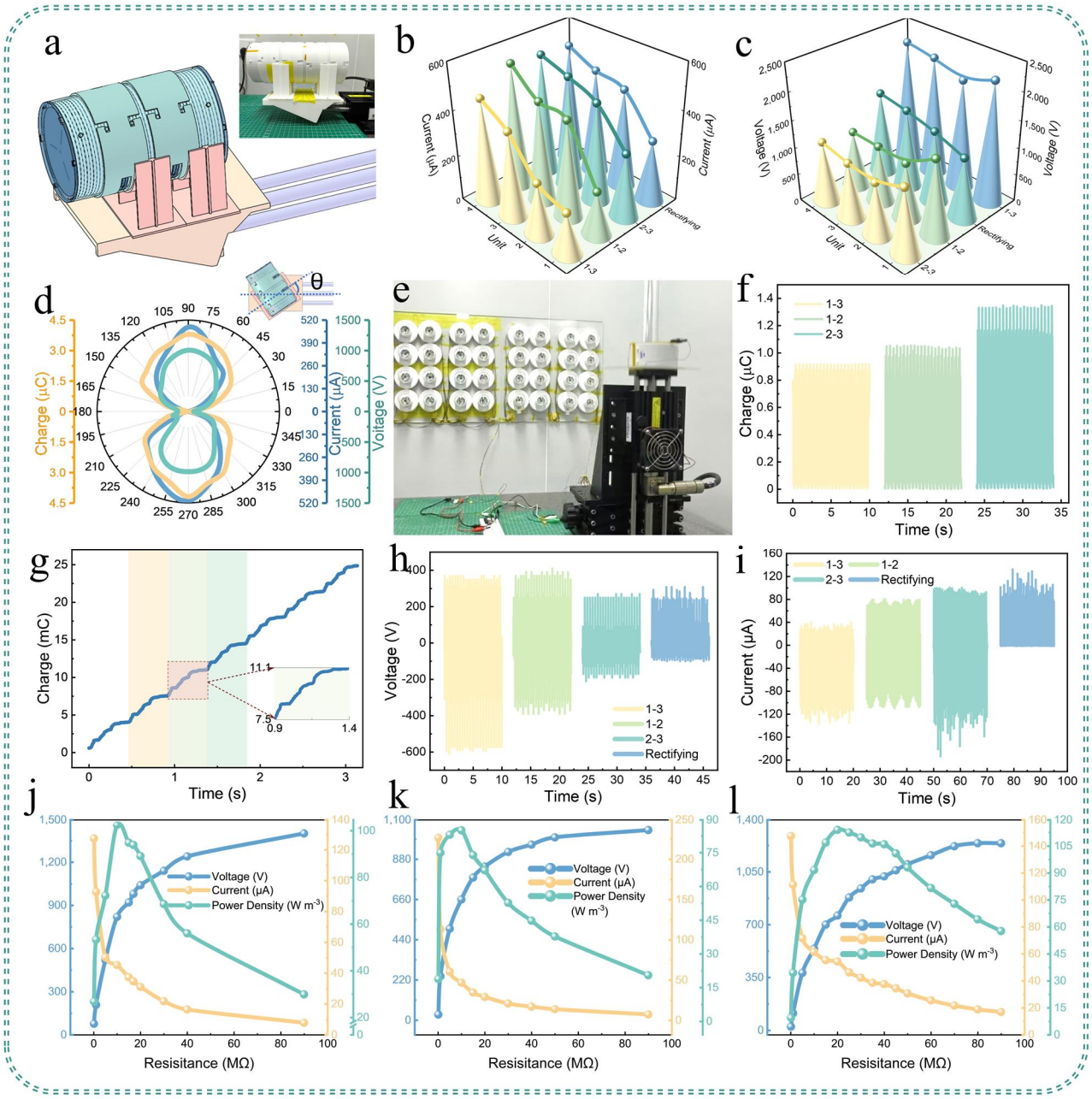

Fig. S23. Output characteristics of RD-TENG for harvesting vibrational energy. (a) Array device vibration energy simulation testing platform (b-c) Under the optimal excitation conditions of frequency 2.4 Hz and amplitude 70 mm, the output relationship of short-circuit current and open-circuit voltage with the increase in the number of device arrays. (d) The output relationship of the 1-2 electrode pair for three devices within the array under optimal excitation conditions concerning the variation of azimuth angle. (e-i) Vertical test platform and short-circuit transfer charge, open-circuit voltage, and short-circuit current of each electrode pair in vertical testing. (j-l) Output voltage, current, and peak power density of RD-TENG with different load resistances for the 1-2, 2-3, and rectified electrode pairs.

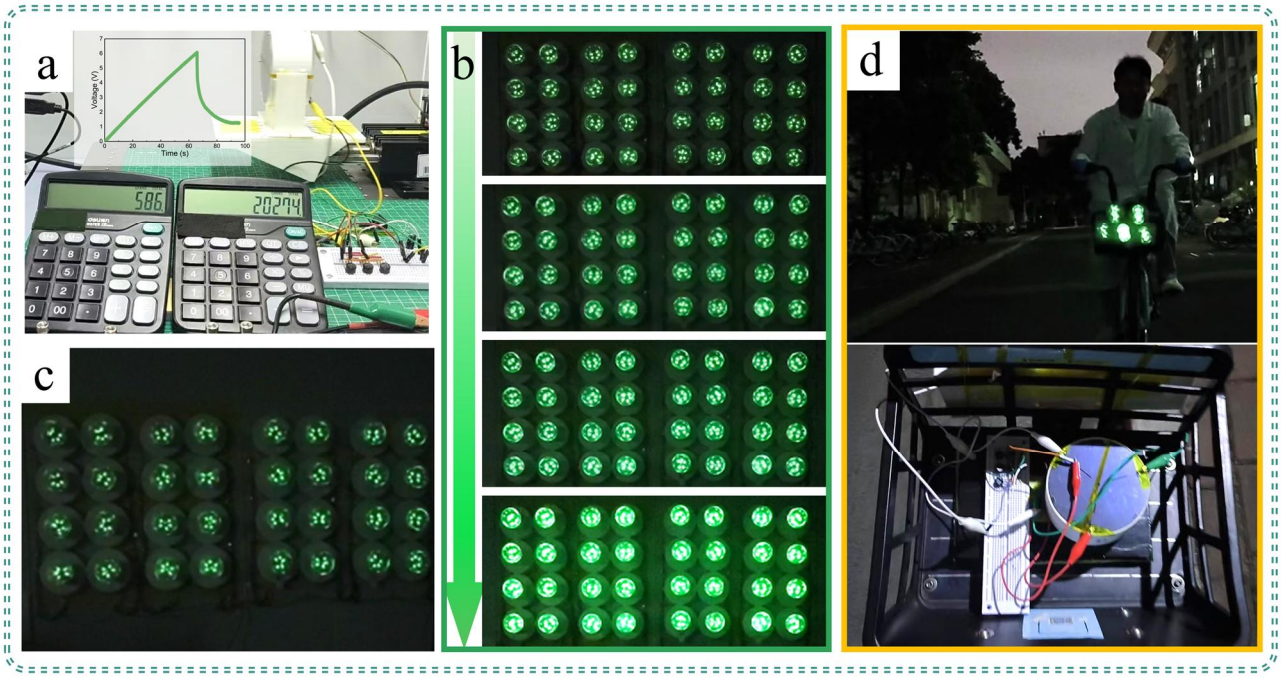

Fig. S24. Application of RD-TENG for vibration energy harvesting. (a) One RD-TENG device charges a 100 μF capacitor for 100 seconds, drives two parallel calculators with continuous power supply for 15 seconds. (b) Schematic diagram showing the lighting of 32 2 W LED bulbs from dim to bright by adding 1 to 4 devices in sequence in the array under the optimal combination of 2.4 Hz frequency and 70 mm amplitude. (c) RD-TENG illuminates 32 2W LED bulbs under vertical drive. (d) The rectifier electrode pair of a single RD-TENG device is placed in the bicycle front basket, driving five 2W commercial LED bulbs as a front light or warning light for the bicycle, providing safety warnings for night rides.

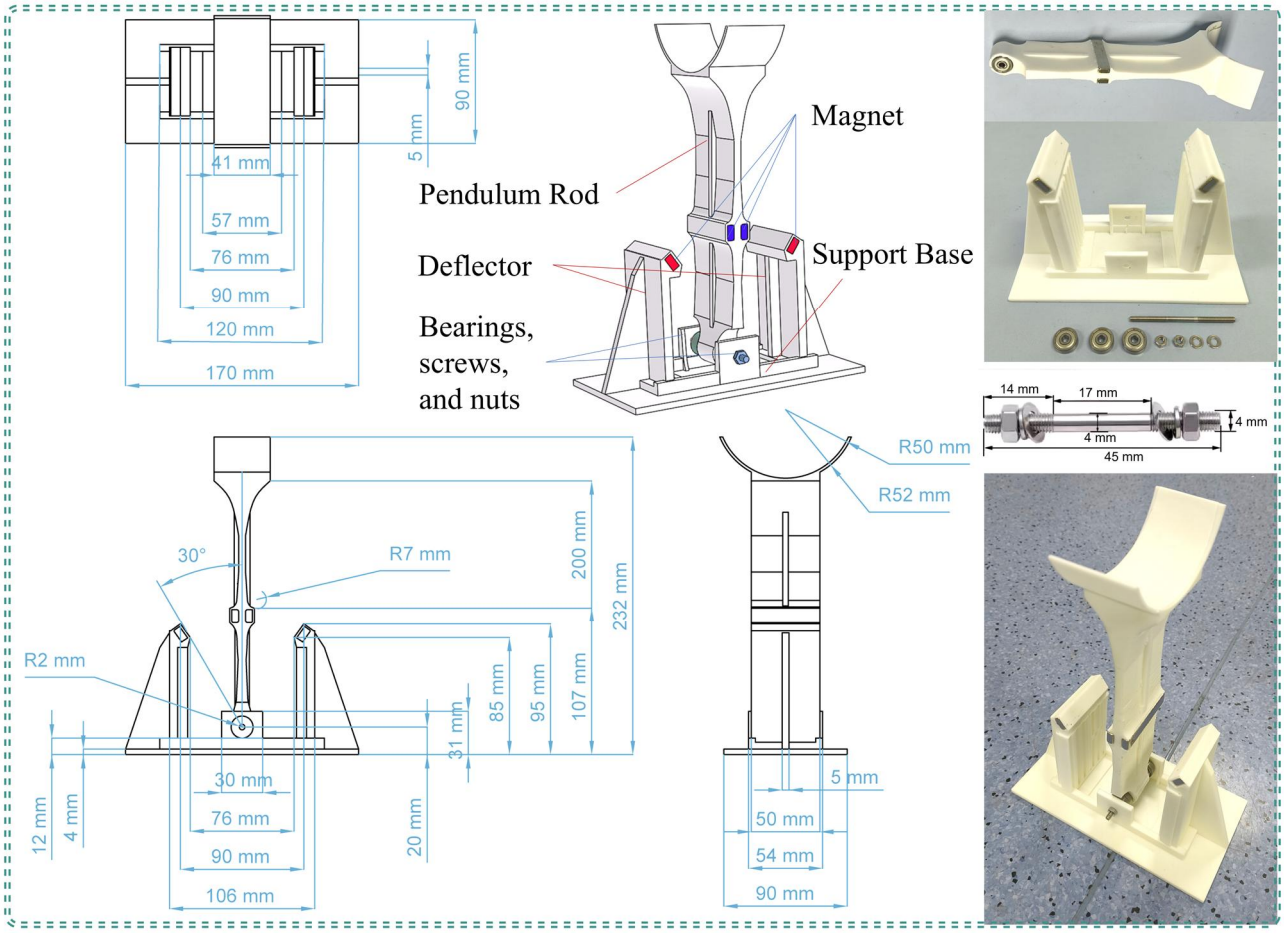

Fig. S25. Dimensional parameters and schematic diagram of the components of frequency-reducing and amplitude-amplifying magnetic repulsion pendulum.

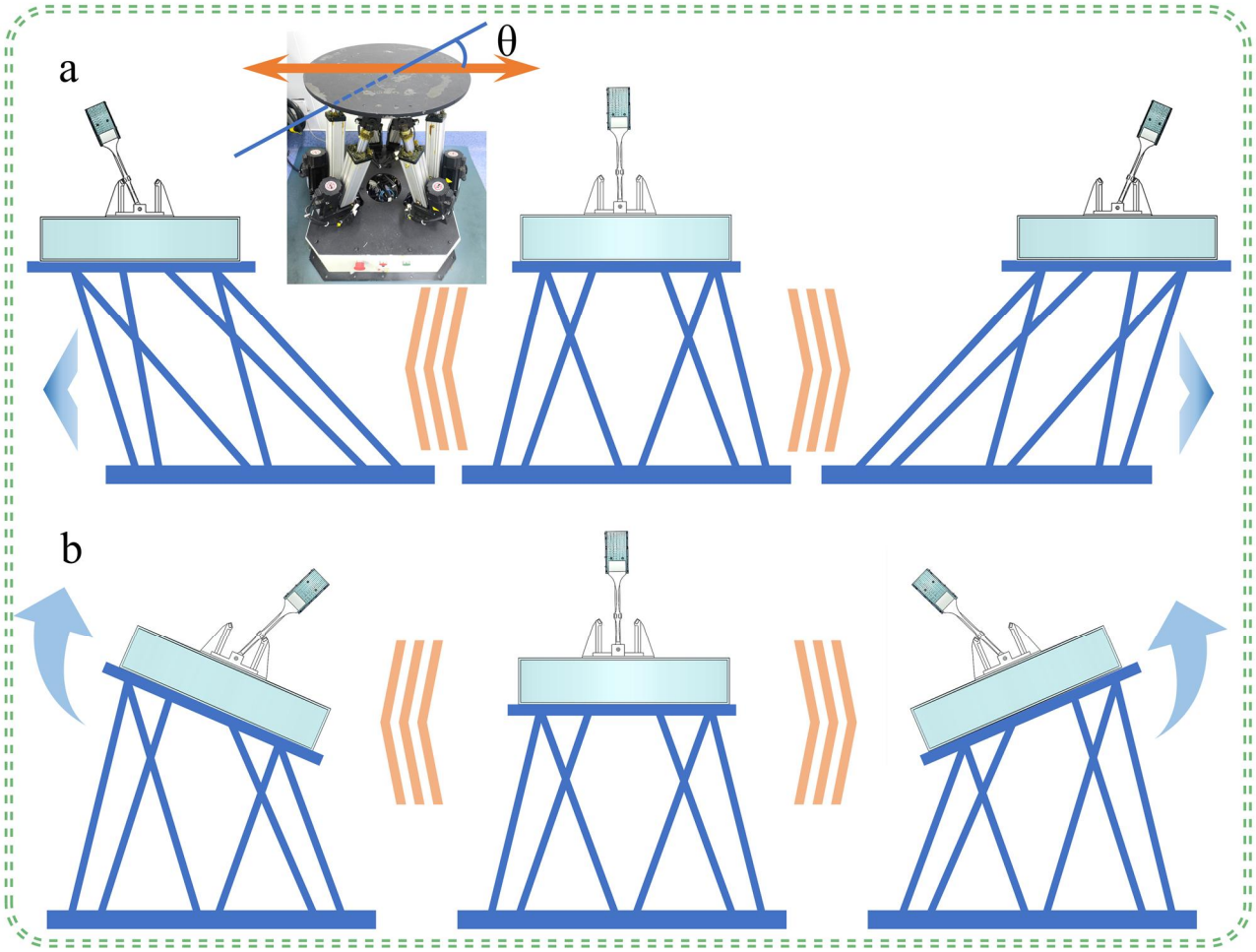

Fig. S26. RD-TENG based on frequency-reducing and amplitude-amplifying magnetic repulsion pendulum driven by a six-degree-of-freedom platform. (a) linear drive. (b) swinging drive.

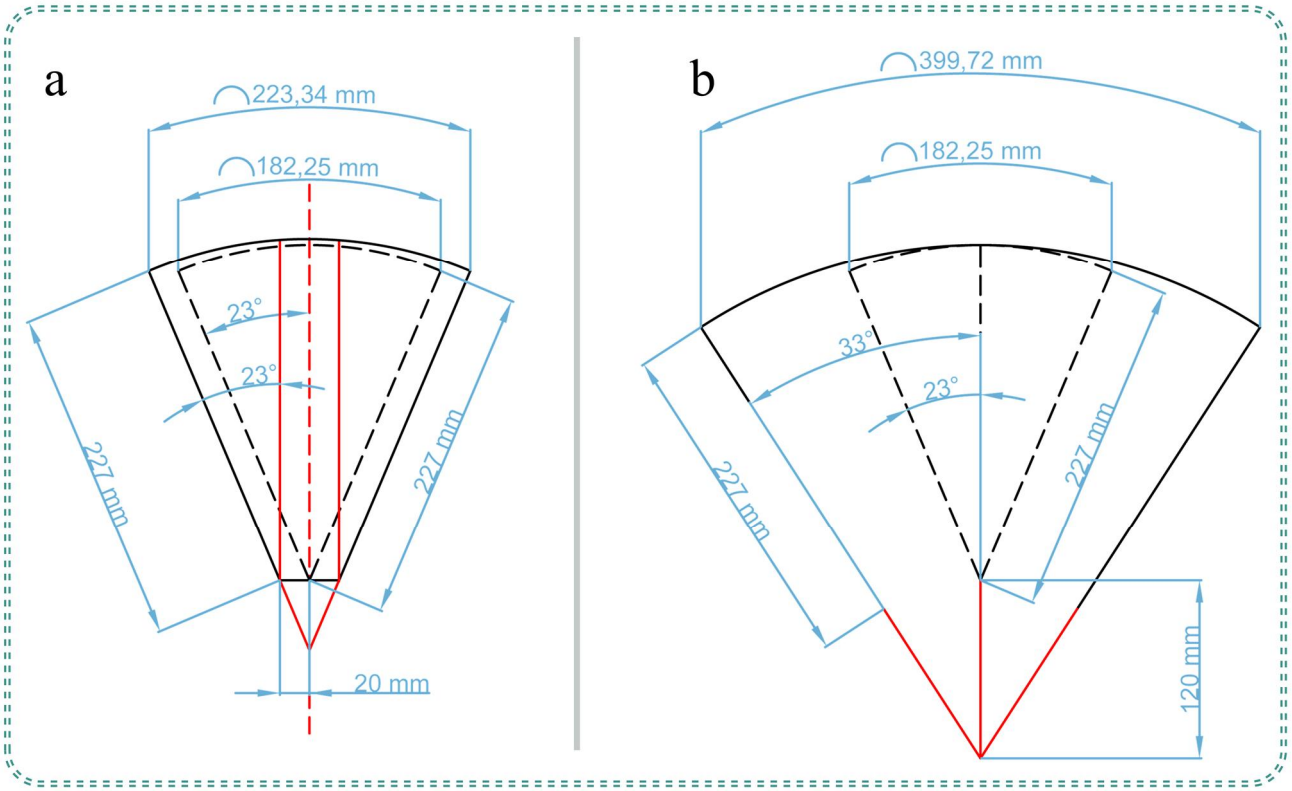

Fig. S27. Amplitude amplification calculation diagram of frequency-reducing and amplitude-amplifying magnetic repulsion pendulum under linear and swinging drive. (a) linear drive. (b) swinging drive.

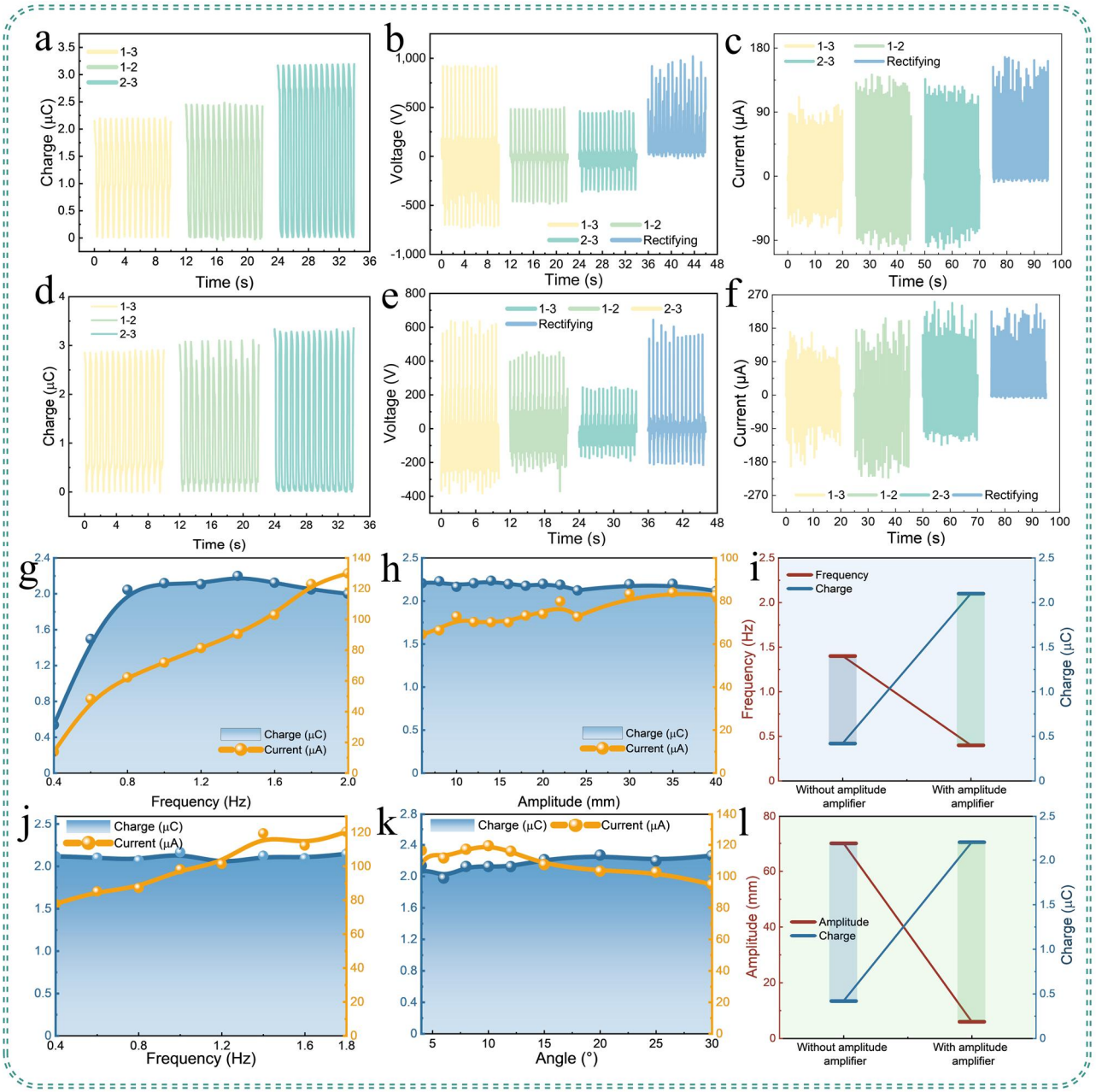

Fig. S28. Output characteristics of RD-TENG based on frequency-reducing and amplitude-amplifying magnetic repulsion pendulum under linear drive and swing drive on a six-degree-of-freedom platform. (a-c) Short-circuit transferred charge, open-circuit voltage, and short-circuit current of each electrode pair under linear drive. (d-f) Short-circuit transferred charge, open-circuit voltage, and short-circuit current of each electrode pair under swinging drive. (g-h) Relationship between output quantities and frequency (Fixed at an amplitude of 70 mm), amplitude (Fixed at a frequency of 2.4 Hz) under linear drive. (i) Frequency reduction and amplitude amplification characteristics under linear drive. (j-k) Relationship between output quantities and frequency (Fixed at an amplitude of 70 mm), amplitude (Fixed at a frequency of 2.4 Hz) under swinging drive. (l) Frequency reduction and amplitude amplification characteristics under swinging drive.

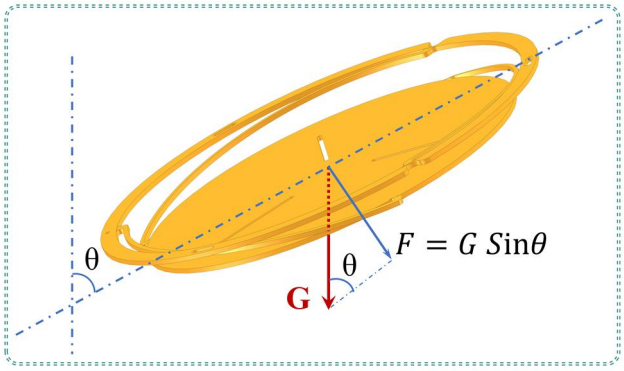

Fig. S29. Force analysis diagram of the vibrating sheet under swinging drive, where a larger swing angle allows the rotor to open more effectively.

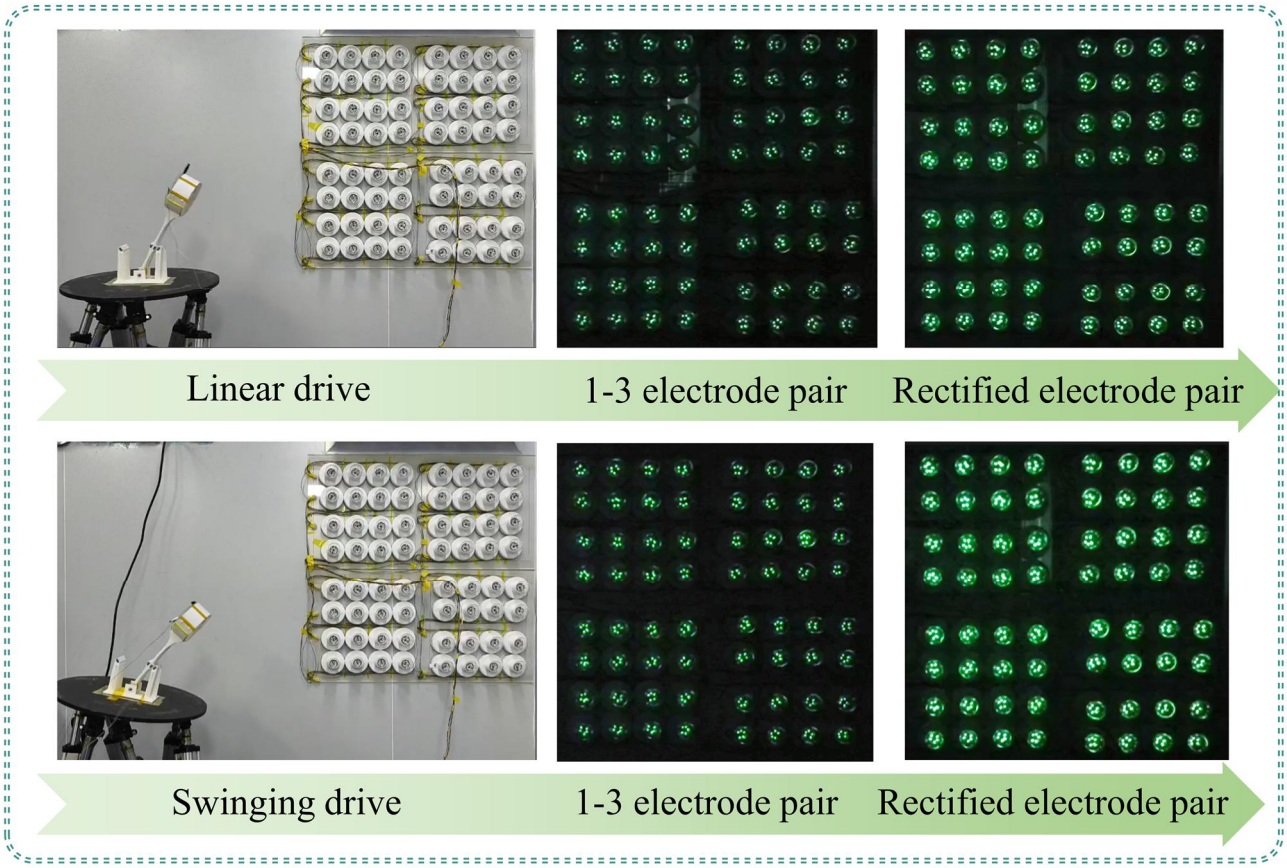

Fig. S30. Comparison of 1-3 and rectified electrode pair lighting up 64 2 W LED bulbs in linear drive and swinging drive mode of RD-TENG based on the frequency-reducing and amplitude-amplifying magnetic repulsion pendulum.

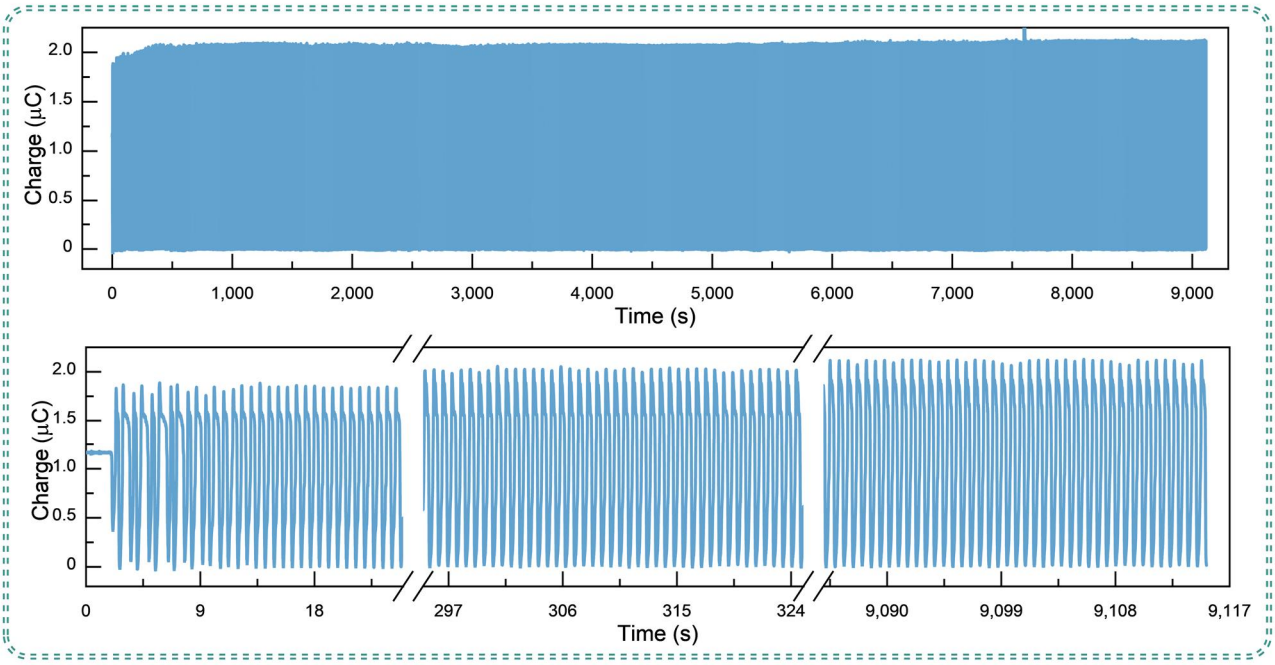

Fig. S31. Durability test of the 1-3 electrode pair of RD-TENG based on low-frequency and amplitude-amplifier of magnetic repulsive pendulum under linear excitation.

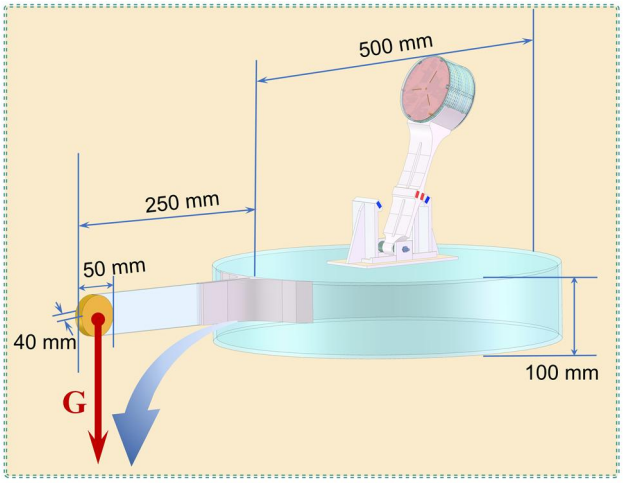

Fig. S32. Diagram of the unbalanced gravity pendulum set on the edge of a buoyant base.

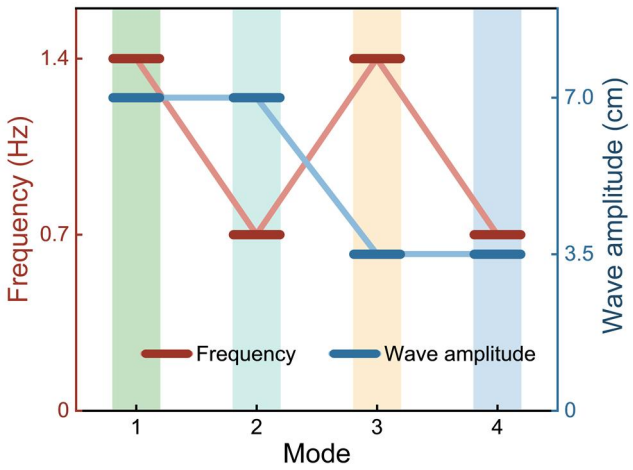

Fig. S33. Wave amplitudes and frequencies generated by different modes in a wave pool.

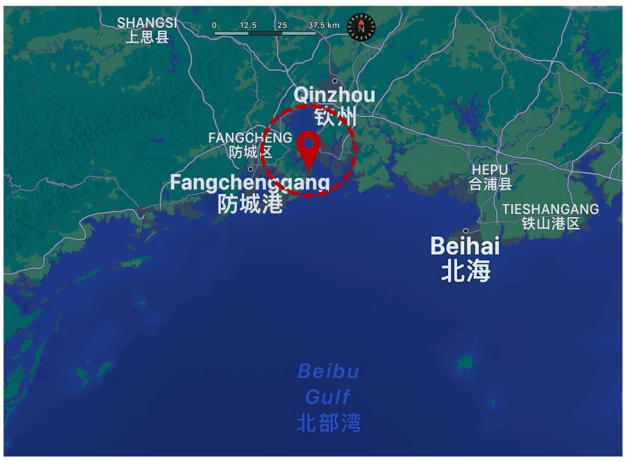

Fig. S34. Satellite location map of the Beibu Gulf test base.